

1 Lower-tropospheric CO₂ from near-infrared ACOS-GOSAT 2 observations

3
4 Susan S. Kulawik¹, Chris O'Dell², Vivienne H. Payne³, Le Kuai⁴, Helen M.
5 Worden⁵, Sebastien C. Biraud⁶, Colm Sweeney⁷, Britton Stephens⁷, Laura T.
6 Iraci⁸, Emma L. Yates¹, Tomoaki Tanaka⁸

7
8 (1) Bay Area Environmental Research Institute, Sonoma, CA, USA

9 (2) Cooperative Institute for Research in the Atmosphere, Colorado State
10 University, Fort Collins, CO, USA

11 (3) Jet Propulsion Laboratory, California Institute of Technology, Pasadena,
12 CA, USA

13 (4) UCLA Joint Institute for Regional Earth System Science and Engineering
14 (JIFRESSE), Los Angeles, CA, USA

15 (5) Atmospheric Chemistry Observations & Modeling (ACOM) Laboratory
16 National Center for Atmospheric Research, Boulder CO 80307 USA

17 (6) Lawrence Berkeley National Laboratory, Earth Science Division, Berkeley,
18 CA, USA

19 (7) NOAA/ESRL/GMD, Boulder, CO, USA

20 (8) NASA Ames, Moffett Field, CA, USA

21 22 **Abstract**

23 We present two new products from near-infrared GOSAT observations:
24 LowerMost Tropospheric (LMT, from 0-2.5 km) and Upper
25 tropospheric/stratospheric (U, above 2.5 km) carbon dioxide partial column
26 mixing ratios. We compare these new products to aircraft profiles and
27 remote surface flask measurements and find that the seasonal and year-to-
28 year variations in the new partial column mixing ratios significantly improve
29 upon the ACOS-GOSAT initial guess/a priori, with distinct patterns in the LMT
30 and U seasonal cycles which match validation data. For land monthly
31 averages, we find errors of 1.9, 0.7, and 0.8 ppm for retrieved GOSAT LMT,
32 U, and XCO₂; for ocean monthly averages, we find errors of 0.7, 0.5, and
33 0.5 ppm for retrieved GOSAT LMT, U, and XCO₂. In the southern
34 hemisphere biomass burning season, the new partial columns show similar
35 patterns to MODIS fire maps and MOPITT multispectral CO for both vertical
36 levels, despite a flat ACOS-GOSAT prior, and a CO/CO₂ emission factor
37 comparable to published values. The difference of LMT and U, useful for
38 evaluation of model transport error, has also been validated with monthly
39 average error of 0.8 (1.4) ppm for ocean (land). LMT is more locally
40 influenced than U, meaning that local fluxes can now be better separated
41 from CO₂ transported from far away.

42 43 **1 Introduction**

44 The Greenhouse Gases Observing Satellite (GOSAT) has been measuring
45 global satellite CO₂ columns since 2009, achieving less than 0.3 ppm
46 variability in regional biases and 1.7 ppm single observation error versus
47 TCCON (Kulawik et al., 2016), where the error is estimated as described in
48 Table 3. The sensitivity of near-infrared radiances to CO₂ varies by altitude
49 differently in the strong and weak bands, resulting in the capability of
50 retrieving multiple pieces of vertical information from near-infrared
51 observations, with 3+ degrees of freedom (i.e. independent pieces of
52 information) for TCCON (Connor et al., 2016; Kuai et al., 2012), 1.6 degrees
53 of freedom for GOSAT (this paper), and 2.0 degrees of freedom for OCO-2
54 (Kulawik, unpublished result). In this paper we use the intermediate
55 retrieved profile from ACOS-GOSAT processing to construct, bias-correct,
56 and validate two partial column mixing ratios from near-infrared GOSAT
57 observations (schematically shown in Fig. 1). The partially correlated errors
58 and sensitivity of these two partial column volume mixing ratios (or mole
59 fractions) are characterized so that they can be used for flux estimation and
60 other science analyses.

61

62 An important goal of carbon cycle research is to improve top-down estimates
63 of CO₂ fluxes, which assimilate data into models to trace the observed
64 variability in the long-lived tracer backwards to sources and sinks.

65 Historically, such top-down flux estimates have relied on surface
66 observations (e.g. Peters et al., 2007; Chevallier et al., 2010), though it was
67 postulated 15 years ago that satellite-based measurements of column CO₂
68 could dramatically reduce top-down based flux uncertainties (Rayner and
69 O'Brien, 2001; O'Brien and Rayner, 2002). Guided by this early work, most
70 GOSAT analyses have focused solely on total column CO₂ (or XCO₂).

71 Separation of XCO₂ into two vertical columns has several advantages over
72 column XCO₂ and surface observations which should improve our ability to
73 accurately estimate fluxes:

74

75 • flux estimates from column measurements rely on observations up to
76 continent-scales away (Liu et al., 2015; Feng et al., 2016); whereas
77 LMT back-trajectories show a more local influence to surface fluxes,
78 making flux estimates more responsive to observations and less
79 susceptible to transport error, a major driver of flux uncertainties
80 (Houweling et al., 2015; Liu et al., 2015; Chevallier et al., 2014; Liu et
81 al., 2011; Prather et al., 2008)

82 • Stephens et al. (2007) show that vertical gradient in mole fraction
83 determined from 2 points in the atmospheric column better constrains
84 model transport and partitioning between northern extratropical land
85 fluxes and land fluxes further south, since vertical transport is an
86 uncertainty in flux estimates (Deng et al., 2015; Lauvaux and Davis,
87 2014; Stephens et al., 2007)

- In majority of cases the LMT covers the entire boundary layer, which partially mitigates one source of flask assimilation error, the boundary layer height (Denning et al., 1996; Gurney et al., 2002; Rayner and O'Brien, 2001); and
- GOSAT provides observations in many areas that are sparsely covered by surface-based measurements.

In this work, we evaluate the precision and comparability of these new LMT and U partial column products derived from GOSAT, with the goal of providing a higher level of information to the flux inversion estimates than is available from the total column alone. This paper is structured as follows. We introduce the datasets used in Section 2, and the theoretical basis in Section 3. Section 4 describes methodology, e.g. the coincidence criteria and GOSAT bias correction. Section 4.1 uses back-trajectories to estimate the distance to peak sensitivity to surface fluxes for LMT and U. Section 5 shows comparisons to aircraft observations and surface sites, including maps of the two partial column mixing ratios. Section 5.4 shows patterns of the two partial column mixing ratios versus MOPITT multi-spectral CO retrievals, and Section 5.5 looks at errors of LMT minus U. Section 6 discusses and summarizes these results.

2. Datasets

There are two datasets used for validation of the new partial column mixing ratios. Measurements of CO₂ vertical profiles from aircraft profiles, which extend from the surface to somewhere between 5 and 13 km, can be used to directly validate what is seen with the two GOSAT partial column mixing ratios. The second dataset that is used is CO₂ measurements from remote surface flask sites, which are used to compare to the lower GOSAT partial column, assuming that CO₂ mixing ratios in the lower 0-2.5 km are well mixed at remote sites. The Total Carbon Column Observing Network (TCCON), which currently measures full columns, is used to diagnose discrepancies between aircraft and GOSAT at the sites where both exist. We additionally show the southern hemisphere, which has interesting CO₂ patterns, very little structure in the prior, and no observations used in the bias correction. We show patterns from burning and transport in southern hemisphere from vertically resolved GOSAT, vertically resolved MOPITT CO, and MODIS fire counts. Figure 2 shows aircraft and surface validation locations, along with GOSAT coincidences, with the surface site locations and names shown in Table 1.

2.1 GOSAT

The Greenhouse gases Observing SATellite (GOSAT) takes measurements of reflected sunlight in three near-infrared bands with a circular footprint of approximately 10.5 km diameter at nadir (Kuze et al., 2016; Yokota et al.,

132 2009; Crisp et al., 2012). The Atmospheric CO₂ Observations from Space
133 (ACOS) v3.5 processing of GOSAT XCO₂ observations are used from the Lite
134 products, with quality flag of 0 (good), along with the full CO₂ profile, full
135 CO₂ averaging kernel matrix, and full CO₂ error matrices from ancillary
136 GOSAT files. We use both nadir land observations (looking straight down)
137 and ocean glint observations (sunglint tracking mode), but not medium gain
138 over land, as there is not a sufficient amount of co-located validation data to
139 validate medium gain observations.

140

141 **2.2 Aircraft profiles**

142

143 **2.2.1 ESRL aircraft profiles**

144 Aircraft and ocean measurements taken by NOAA's Earth System Research
145 Laboratory (ESRL) are obtained from an observation package product
146 (GLOBALVIEW-CO2,2013; Sweeney et al., 2015).

147

148 **2.2.2 DOE/LBNL aircraft profiles**

149 Aircraft observations collected over the Southern Great Plains can be
150 obtained from DOE ARM archive (www.arm.gov, search for CO₂ flasks at
151 SGP) under ARM-ACME campaigns and are described in Biraud et al. (2013).
152 Flask-based observations are collected on a bi-weekly basis at altitude
153 ranging from 0.2 to 5km.

154

155 **2.2.3 Aircraft profile extension and errors**

156 Aircraft measurements are extended down to the surface using the lowest
157 measured value, and extended to the tropopause pressure using the aircraft
158 value at the highest altitude. The tropopause pressure is used from the
159 National Centers for Environmental Prediction (NCEP),
160 <http://www.esrl.noaa.gov/psd/data/gridded/data.ncep.reanalysis.html>. The
161 CarbonTracker model (CT2015, see below) is used to extend the profile
162 through the stratosphere. The aircraft flask measurements themselves have
163 errors, but these are small compared to the other errors in the comparisons
164 (e.g. co-location, extending the aircraft to the top of the atmosphere, etc.)

165

166 **2.3 Remote NOAA/ESRL oceanic surface in situ measurements**

167 Remote surface sites are from the Earth System Research Laboratory
168 Observation Package Data Product surface flask measurements (Conway et
169 al., 1994). The "remote oceanic" locations used in this paper are selected to
170 have at least 97% ocean along a circle with a 5 degrees radius around the
171 location. The locations are shown in Fig. 2 and Table 1. For each station,
172 there can be different options represented by file names (e.g. daytime,
173 nighttime, representative, etc.); in this study "representative" files are used,
174 with outliers removed, if that option is available. Remote ocean sites have
175 been selected because (a) although the vertical airmass observed by GOSAT

176 LMT will not match the vertical air mass observed by the surface site, the
177 long correlation length scales of remote locations should make the
178 comparisons useful; and (b) these sites are not used in development of the
179 bias correction terms (described in Section 3.5 and Appendix A) and so are
180 an independent test of bias correction for observations over ocean.

181

182 **2.4 HIPPO aircraft profiles**

183 The HIAPER Pole-to-Pole Observations (HIPPO) project samples the
184 atmosphere in a series of profiles from the surface to 9-13 km, from about
185 80N to 60S. The campaigns covered different years as well as different
186 seasons, namely: HIPPO 1: January, 2009, HIPPO 2: November 2009, HIPPO
187 3: March-April, 2010, HIPPO 4: June-July, 2011, and HIPPO 5: August-
188 September, 2011. Frankenberg et al. (2016) recently were successful in
189 evaluating satellite measurements of column CO₂ over ocean (including
190 GOSAT) using HIPPO. In this paper, we look at comparisons between GOSAT
191 and HIPPO 2-5 (HIPPO 1 occurs prior to GOSAT launch) using the HIPPO-
192 identified profiles and the CO₂_X field, based on 1s data averaged to 10s,
193 from two (harmonized) sensors: CO₂-QCLS and CO₂-OMS. Due to the
194 GOSAT glint coverage span of about 40 degrees, and after applying quality
195 screening, many of the comparisons had fairly limited latitudinal spans with
196 the GOSAT improvement over the prior found more in improving the bias
197 rather than improving the standard deviation. The combined campaigns
198 span a wide range of GOSAT latitudes.

199

200 **2.5 AJAX aircraft profiles**

201 The Alpha Jet Atmospheric eXperiment (AJAX) project
202 (<https://earthscience.arc.nasa.gov/ajax>) collects in situ CO₂ vertical profiles
203 from the surface to 8 km in several locations, including Railroad Valley, NV;
204 Merced, CA, and other locations in the West Coast. Most of the AJAX Version
205 4 profiles used in this paper were collected to coincide with GOSAT
206 overpasses. Trace gas instruments and the Meteorological Measurement
207 Sensor are housed in an unpressurized sensor pod that is mounted under
208 the wing. A cavity ring-down spectrometer (Picarro Inc. G2301-m) that has
209 been modified for flight conditions is routinely calibrated to NOAA/ESRL gas
210 standards. Calculated 1 σ overall uncertainties are 0.16 ppm for CO₂ (Hamill
211 et al. 2016; Tanaka et al., 2016).

212

213 **2.6 MOPITT v6 multispectral CO retrieval**

214 In section 5, we utilize satellite-based CO observations from MOPITT to
215 understand the spatial variability in LMT and U that may be attributed to
216 fires. The MOPITT instrument on EOS-Terra is in a sun-synchronous orbit
217 with mean local time overpasses of 10:30 and 22:30. It has global coverage
218 in \sim 3 days with a 22km x 22km horizontal footprint. MOPITT uses gas filter
219 correlation radiometry (GFCR) to measure atmospheric CO at 4.6 μ m

220 (Thermal Infrared) and 2.3 μm (Short-wave Infrared) and is the only
221 satellite instrument capable of simultaneous multispectral retrievals of CO
222 with enhanced sensitivity to near-surface CO for daytime/land observations
223 (Worden et al., 2010). MOPITT CO data have been validated for each
224 retrieval algorithm version using aircraft in situ measurements (Deeter et
225 al., 2014). Here we use daytime only MOPITT V6J (multispectral) data that
226 have been filtered to require cloud free scenes from both MOPITT and
227 MODIS cloud detection. We also use a measure of sensitivity to near-surface
228 CO computed from the trace of the averaging kernel for the lowest 200 hPa
229 of the atmosphere to select scenes that contain relatively more information
230 from the measurement.

231

232 **2.7 MODIS fire counts**

233 MODIS fire counts (found at [https://lance.modaps.eosdis.nasa.gov/cgi-](https://lance.modaps.eosdis.nasa.gov/cgi-bin/imagery/firemaps.cgi)
234 [bin/imagery/firemaps.cgi](https://lance.modaps.eosdis.nasa.gov/cgi-bin/imagery/firemaps.cgi)) are used to identify biomass burning locations.
235 Fire maps are created by Jacques Descloitres with fire detection algorithm
236 developed by Louis Giglio. Blue Marble background image created by Reto
237 Stokli (Giglio et al., 2003; Davies et al., 2004).

238

239 **2.8 CarbonTracker model**

240 CarbonTracker CT2015, <http://carbontracker.noaa.gov>, (Peters et al., 2007)
241 is used to extend aircraft profiles from the stratosphere to the top of the
242 atmosphere (similarly to in Frankenberg et al., 2016 and Inoue et al., 2013)
243 and to quantify co-location error (similarly to Kulawik et al. (2016)).

244

245 **2.9 TCCON**

246 The Total Carbon Column Observing Network (TCCON) observations, version
247 GGG2014 (Wunch et al., 2011a) at Lamont (Wennberg et al., 2014) and
248 Park Falls (Wennberg et al., 2014), where both aircraft and TCCON
249 observations have co-located measurements, are used to evaluate XCO₂
250 calculated from the aircraft observations (extended as described by Section
251 3.7). Although the TCCON observations contain information that allow each
252 measurement to be split into 2 or 3 vertical columns, the focus of the TCCON
253 project has been on column observations of CO₂ (and columns of other trace
254 gases). Recent work by Kuai et al. (2012), Dohe et al. (2012), and Connor
255 et al. (2016) have explored vertical profile retrievals from TCCON, but there
256 is not yet an operational product.

257

258 **2.10 AirCore**

259 While the boundary layer and lower free troposphere are relatively well
260 sampled by a network of insitu and flask measurements over the globe, the
261 UT/LS is rarely sampled due to the expense and the difficulty involved in
262 making measurements at these altitudes. The recent advent of the AirCore
263 (Karion et al., 2010; Membrive et al., 2016) has enable more frequent

264 profiles that sample as high as 30 km, well into the stratosphere. Profiles in
265 this study were dried with MgClO₄ and captured in a long stainless steel
266 coated with thin silicate layer (Silconert 1000) and later (within 3 hours of
267 sampling) analyzed for CO₂/CH₄/CO. Given the 3 hour time interval between
268 sampling and analysis of the AirCore and the fact that the average rate of
269 molecular diffusion of CO₂ the resolution of the AirCore is better than 1kPa
270 for the bottom 95% of the atmospheric column. AirCores were used in
271 Appendix A to estimate the error incurred by extending NOAA/ESRL aircraft
272 CO₂ profiles above 6 km.

273

274 **3.0 LMT and U theoretical basis**

275 In Section 3.1, equations are presented describing the sensitivity and errors
276 of the new products. In Section 3.2, a simulation is shown of what GOSAT is
277 expected to see from space using the developed equations and aircraft
278 profiles from the Southern Great Plains (SGP) aircraft site.

279

280 **3.1 Equations describing sensitivity and errors**

281 The ACOS retrievals (O'Dell et al., 2012) utilize an optimal estimation
282 approach with a priori constraints (Rodgers, 2000). It is common practice to
283 represent the state parameter to be retrieved on an altitude grid that is finer
284 than the altitude resolution of the instrument (e.g., Bowman et al., 2006;
285 Deeter et al., 2003; von Clarmann et al., 2003). A major advantage of this
286 approach is that it allows the calculation of diagnostics, such as averaging
287 kernels, which can be used to characterize the sensitivity of the
288 measurement. Constraints (regularization) must be applied in order to
289 stabilize the retrieval (e.g., Rodgers, 2000; Tikhonov, 1963; Twomey, 1963;
290 Steck and von Clarmann, 2001; Kulawik et al., 2006). The constraints may
291 be chosen to constrain absolute values and/or the shape of the retrieved
292 result.

293

294 In the ACOS processing, CO₂ is first retrieved as a 20-level profile, where the
295 GOSAT pressure levels are sigma levels with the 5th level approximately 2.5
296 km above the surface. The retrieved CO₂ profile averages 1.6 degrees of
297 freedom (DOF) with about 0.8 DOF for levels 16-20 (where level 20 is the
298 surface) and 0.8 DOF for levels 1-15 (where level 1 is at the top of the
299 atmosphere). This intermediate profile has significant altitude-dependent
300 biases and cannot be used scientifically as-is, but rather this profile is
301 compacted to a single column quantity, XCO₂ as the final step in the ACOS
302 processing. In this work, we post-process the ACOS-GOSAT intermediate
303 profile to calculate and characterize the partial column mixing ratio
304 represented by levels 16-20, which is named LMT_XCO₂ or LMT for short,
305 and the partial column mixing ratio represented by levels 1-15, which is
306 named U_XCO₂ or U for short. The two partial columns each have about

307 0.8 degrees of freedom, meaning that they will each capture about 80% of
308 the true variability of their partial column.

309
310 The equation for the linear estimate of \mathbf{x} , the retrieved CO₂ profile (Connor
311 et al., 2008; Rodgers, 2000) is:

$$312 \hat{\mathbf{x}} = \mathbf{x}_a + \mathbf{A}_{xx}(\mathbf{x}_{true} - \mathbf{x}_a) + \mathbf{A}_{xv}(\mathbf{v}_a - \mathbf{v}_{true}) + \mathbf{G}_x \boldsymbol{\varepsilon} \quad (1)$$

314
315 Where

- 316 • \mathbf{x} is the retrieved CO₂ profile, size n_{CO_2} (20 for ACOS-GOSAT)
- 317 • \mathbf{x}_a is the a priori profile, size n_{CO_2}
- 318 • \mathbf{x}_{true} is the true value, size n_{CO_2}
- 319 • \mathbf{A}_{xx} is the $n_{CO_2} \times n_{CO_2}$ CO₂ profile averaging kernel
- 320 • $\mathbf{A}_{xv}(\mathbf{v}_a - \mathbf{v}_{true})$ is the cross-state error representing the propagation of
321 error from non-CO₂ retrieved parameters, \mathbf{v} (aerosols, albedo, etc.),
322 into retrieved CO₂. This variable is called " \mathbf{u} " in Connor et al., 2008.
- 323 • \mathbf{v}_a is the interferent value (used to generate fit radiances), size n_{interf} .
324 For ACOS-GOSAT n_{interf} is 26(27) for ocean(land)
- 325 • \mathbf{v}_{true} is the true interferent value, size n_{interf}
- 326 • \mathbf{A}_{xv} is size $n_{CO_2} \times n_{interf}$
- 327 • \mathbf{G}_x is the gain matrix, size $n_{CO_2} \times n_s$, where n_s is the number of spectral
328 points, and
- 329 • $\boldsymbol{\varepsilon}$ is the spectral error, size n_s

330
331 The pressure weighting function, " \mathbf{h} " (size n_{CO_2}) is used to convert the
332 retrieved CO₂ profile to XCO₂ by tracking each level's contribution to the
333 column quantity.

$$334 \mathbf{h}_{x_{CO_2}}^T = [0.026 \ 0.053 \ 0.053 \ 0.053 \ \dots \ 0.053 \ 0.053 \ 0.053 \ 0.026] \quad (2a)$$

336
337 The sensitivity to the top or bottom level is half that of other levels, as these
338 levels contribute to only one layer, rather than two adjacent layers. The
339 GOSAT levels are chosen such that the pressure weighting is very similar for
340 all layers and all observations. However, the pressure weighting is not
341 identical for all layers and all observations and the values used in our
342 analysis are the actual values in the files, with average values shown here,
343 rounded to 2 significant digits.

344
345 The LMT pressure weighting function is obtained by starting with the
346 pressure weighting function for XCO₂, setting levels 1-15 to zero, then
347 normalizing so that the sum of all entries adds to 1. For the U pressure
348 weighting function, levels 16-20 are set to zero, then the vector is
349 normalized so that the sum is 1. The LMT and U pressure weighting
350 functions are:

351
352 $\mathbf{h}_{LMT}^T = [0 \ 0 \ 0 \ 0 \ \dots \ 0 \ 0.22 \ 0.22 \ 0.22 \ 0.22 \ 0.11]$ (2b)

353 $\mathbf{h}_U^T = [0.035 \ 0.069 \ 0.069 \ \dots \ 0.069 \ 0.069 \ 0 \ 0 \ 0 \ 0 \ 0]$ (2c)

354

355 To calculate XCO₂, the equation is:

356

357 $XCO_2 = \mathbf{h}_{XCO_2}^T \cdot \hat{\mathbf{x}}$ (3)

358

359 The fraction of total air in each of the partial columns average:

360

361 $f_{XCO_2} = 1$ (4a)

362 $f_{LMT} = 0.235$ (4b)

363 $f_U = 0.765$ (4c)

364

365 Combining Eqs. 1, 2a, and 3, the XCO₂ estimate is:

366

367 $\mathbf{X}\hat{\mathbf{C}}O_2 = \mathbf{X}CO_{2a} + \mathbf{h}_{XCO_2}^T \mathbf{A}_{xx} (\mathbf{x}_{true} - \mathbf{x}_a) + \mathbf{h}_{XCO_2}^T \mathbf{A}_{xv} (\mathbf{v}_{true} - \mathbf{v}_a) + \mathbf{h}_{XCO_2}^T \mathbf{G}_x \boldsymbol{\varepsilon}$ (5a)

368 $\mathbf{X}\hat{\mathbf{C}}O_2 = \mathbf{X}CO_{2a} + \mathbf{a}_{xx} (\mathbf{x}_{true} - \mathbf{x}_a) + \mathbf{a}_{xv} (\mathbf{v}_{true} - \mathbf{v}_a) + \mathbf{g}_x \boldsymbol{\varepsilon}$ (5b)

369

370 where \mathbf{a}_{xx} is the column averaging kernel, $\mathbf{a}_{xx} = \mathbf{h}_{XCO_2}^T \mathbf{A}_{xx}$ (see Appendix A of
371 Connor, 2008).

372

373 Similarly, to calculate the linear estimate for the 2-vector [LMT, U], Equation
374 1 is multiplied by the 2 x n_{CO_2} pressure weighting function, $\mathbf{h} = [\mathbf{h}_{LMT}, \mathbf{h}_U]$:

375

376 $\begin{pmatrix} L\hat{M}T \\ \hat{U} \end{pmatrix} = \begin{pmatrix} LMT \\ U \end{pmatrix}_a + \mathbf{h}^T \mathbf{A}_{xx} (\mathbf{x}_{true} - \mathbf{x}_a) + \mathbf{h}^T \mathbf{A}_{xv} (\mathbf{v}_{true} - \mathbf{v}_a) + \mathbf{h}^T \mathbf{G}_x \boldsymbol{\varepsilon}$ (6a)

377 $\begin{pmatrix} L\hat{M}T \\ \hat{U} \end{pmatrix} = \begin{pmatrix} LMT \\ U \end{pmatrix}_a + \mathbf{a}_{xx} (\mathbf{x}_{true} - \mathbf{x}_a) + \mathbf{a}_{xv} (\mathbf{v}_{true} - \mathbf{v}_a) + \mathbf{g}_x \boldsymbol{\varepsilon}$ (6b)

378

379 where now $\mathbf{a}_{xx} = [\mathbf{h}_{LMT}, \mathbf{h}_U]^T \mathbf{A}_{xx}$, a (2 x n_{CO_2}) matrix, $\mathbf{a}_{xv} = [\mathbf{h}_{LMT}, \mathbf{h}_U]^T \mathbf{A}_{xv}$, a 2 by
380 n_{interf} matrix, and $\mathbf{g}_x = [\mathbf{h}_{LMT}, \mathbf{h}_U]^T \mathbf{G}_x$, a (2 x n_s) matrix.

381

382 The last two terms in Eq. 6 represent the cross-state and measurement
383 error, respectively, and are often jointly called the observation error
384 (Worden et al., 2004). The error in [LMT, U] is estimated by taking the

385 covariance of $\begin{pmatrix} L\hat{M}T \\ \hat{U} \end{pmatrix} - \begin{pmatrix} LMT \\ U \end{pmatrix}_{true}$, a (2 x 2) matrix. The errors can be

386 calculated either from taking the covariance (6a) or from (6b). The
387 covariance of (6a) has a fairly simple form, in terms of the standard
388 definitions of the error covariances for the full profile, \mathbf{S}_{interf} , and \mathbf{S}_{meas} ,
389 which are included in the ACOS-GOSAT ancillary products, and $\mathbf{S}_{smoothing}$ can
390 be calculated from the standard equation, $\mathbf{S}_{smoothing} = (\mathbf{I} - \mathbf{A}) \mathbf{S}_a (\mathbf{I} - \mathbf{A})^T$

391 (Rodgers, 2000), with \mathbf{A} the ($n_{CO_2} \times n_{CO_2}$) CO₂ profile averaging kernel and
 392 \mathbf{S}_a the a priori covariance, both included in the ACOS-GOSAT products.

$$394 \sigma^2_{[LMT,U]} = \mathbf{h}^T \mathbf{S}_{\text{smoothing}} \mathbf{h} + \mathbf{h}^T \mathbf{S}_{\text{interfer}} \mathbf{h} + \mathbf{h}^T \mathbf{S}_{\text{meas}} \mathbf{h} \quad (7a)$$

$$395 = \begin{pmatrix} \mathbf{h}_{lmt}^T \mathbf{S}_{smooth} \mathbf{h}_{lmt} & \mathbf{h}_{lmt}^T \mathbf{S}_{smooth} \mathbf{h}_U \\ \mathbf{h}_U^T \mathbf{S}_{smooth} \mathbf{h}_{lmt} & \mathbf{h}_U^T \mathbf{S}_{smooth} \mathbf{h}_U \end{pmatrix} + \begin{pmatrix} \mathbf{h}_{lmt}^T \mathbf{S}_{obs} \mathbf{h}_{lmt} & \mathbf{h}_{lmt}^T \mathbf{S}_{obs} \mathbf{h}_U \\ \mathbf{h}_U^T \mathbf{S}_{obs} \mathbf{h}_{lmt} & \mathbf{h}_U^T \mathbf{S}_{obs} \mathbf{h}_U \end{pmatrix} \quad (7b)$$

$$396 = \begin{pmatrix} \sigma_{LMT}^2 & c \cdot \sigma_{LMT} \sigma_U \\ c \cdot \sigma_{LMT} \sigma_U & \sigma_U^2 \end{pmatrix} \quad (7c)$$

397
 398 Equation 7 estimates the predicted errors for LMT and U, where $\sigma_{[LMT,U]}$ is a
 399 (2 x 2) matrix. The diagonals are the square of the predicted error for each
 400 parameter, and the off diagonals also depend on the correlated error, c ,
 401 between these parameters. Table 2 shows the predicted errors for LMT, U,
 402 and the error correlation between LMT and U. The predicted errors in Table
 403 2 are larger than the actual errors, as seen later in Tables 4 and 5; error for
 404 averaged observations is estimated in section 4.1.1. The a priori errors,
 405 calculated from $\sigma^2 = \mathbf{h}^T \mathbf{S}_a \mathbf{h}$ are 34 and 9 ppm for LMT and U, respectively,
 406 which are much larger than the posterior errors, indicating that these
 407 quantities are largely unconstrained by the retrieval's prior assumption.

408
 409 Through the same process as Eqs 6-7, the XCO₂ error is:

$$411 \sigma_{XCO_2} = \mathbf{h}_{XCO_2}^T \mathbf{S}_{smooth} \mathbf{h}_{XCO_2} + \mathbf{h}_{XCO_2}^T \mathbf{S}_{obs} \mathbf{h}_{XCO_2} \quad (8)$$

412
 413 XCO₂ can also be calculated as a function of LMT and U, and the XCO₂ errors
 414 can be calculated as a function of the errors in [LMT, U]. These are shown in
 415 Eq. 9.

$$416 \quad 417 XCO_2 = f_{lmt} LMT_CO_2 + f_u U_CO_2 \quad (9a)$$

$$418 \quad 419 \sigma_{XCO_2} = \sqrt{\begin{pmatrix} f_{lmt} & f_u \end{pmatrix} \begin{pmatrix} \sigma_{lmt}^2 & \sigma_{lmt} \sigma_u corr \\ \sigma_{lmt} \sigma_u corr & \sigma_u^2 \end{pmatrix} \begin{pmatrix} f_{lmt} \\ f_u \end{pmatrix}} \quad (9b)$$

$$420 \quad 421 \sigma_{XCO_2} = \sqrt{0.23^2 \sigma_{lmt}^2 + \sigma_u^2 0.77^2 + 2 * 0.77 * 0.23 \sigma_{lmt} \sigma_u corr} \quad (9c)$$

422
 423 where f_{LMT} and f_U are the air masses for the LMT and U partial columns
 424 (0.236, 0.764), respectively, σ_{lmt} is the error for LMT, and $corr$ is the error
 425 correlation between LMT and U.

426
 427 The normalized column averaging kernel is used to see the sensitivity of the
 428 column to the true state at different levels, with a value of 1 meaning
 429 perfect sensitivity, and a value of 0 meaning no sensitivity. The normalized

430 column averaging kernel is the column averaging kernel, \mathbf{a} , divided by the
431 pressure weighting function for each layer, $\mathbf{h}_{\text{XCO}_2}$, and multiplied by the
432 fraction of air in the partial column.

$$433 \mathbf{a}_{\text{normLMT}}[i] = (\mathbf{h}_{\text{LMT}}[i] \mathbf{A}_{\text{CO}_2}[i,j]) / \mathbf{h}_{\text{XCO}_2}[j] * f_{\text{LMT}} \quad (10a)$$

$$435 \mathbf{a}_{\text{normU}}[i] = (\mathbf{h}_{\text{U}}[i] \mathbf{A}_{\text{CO}_2}[i,j]) / \mathbf{h}_{\text{XCO}_2}[j] * f_{\text{U}} \quad (10b)$$

436
437 Figure 3 shows the normalized column averaging kernels for LMT, U, and
438 XCO₂ for a land scene. The ocean averaging kernel is very similar. Although
439 the LMT partial column mixing ratio sums the 5 levels within about 2.5 km of
440 the ground, the LMT has some sensitivity to the true state at all 20 levels
441 because the GOSAT radiances are not able to fully resolve between CO₂
442 within the surface to 2.5 km versus above this. As expected, the sensitivity
443 for LMT plus U is equal to the sensitivity for XCO₂, and the sensitivity for LMT
444 is weighted to the surface whereas the sensitivity for U is weighted to the
445 top of the atmosphere. The negative averaging kernels for LMT in the
446 stratosphere are partially a consequence of the ACOS prior constraint, which
447 does not allow stratospheric variability. Actual stratospheric variability is
448 transferred to the closest levels that are allowed to vary, and the surface
449 compensates for the radiance error induced by this, resulting in a negative
450 sensitivity of the LMT to the true state in the stratosphere. If the
451 stratospheric truth matches that of the *a priori*, then there will be no
452 propagation of error into LMT or U. The averaging kernels shown in Fig. 3
453 are similar to those calculated for TCCON in Fig. 2 of Connor et al. (2016).
454 As seen in Fig. 3, the quantity LMT + U (i.e. XCO₂) has a sensitivity of 1
455 between the surface and 600 hPa, with sensitivity dropping off slowly with
456 altitude above 600 hPa. The 0.8 degrees of freedom for LMT indicates the
457 sensitivity of the retrieved LMT to the true LMT. The missing 0.2 degrees of
458 freedom indicates sensitivity to the prior and/or sensitivity to the U part of
459 the true profile. Since the sensitivity of LMT and U together is 1 near the
460 surface, it is mainly sensitivity to the U part of the true profile. Similarly the
461 0.8 degrees of freedom for U indicates some sensitivity to the LMT and some
462 sensitivity to the U prior.

463 464 **3.2 Seasonal behavior of LMT, U, and XCO₂ estimated using only** 465 **aircraft measurements and GOSAT sensitivity (no GOSAT** 466 **observations)**

467 This section answers the following questions:

- 468 (1) Do U and LMT have unique seasonal signatures?
- 469 (2) How much of the XCO₂ variability is due to LMT versus U
470 variability?
- 471 (3) How much does the prior influence the LMT and U retrievals?

472

473 This section simulates GOSAT retrievals using the linear estimate given the
474 aircraft in situ profiles at the SGP site (37N, 95W), the GOSAT prior, and the
475 GOSAT averaging kernels. This analysis assumes that the CO₂ profile
476 measured by aircraft at SGP (extended by the CarbonTracker model above
477 5.5 km) is the true CO₂ profile, which is then plugged into Eqs. 5 and 6 to
478 calculate the LMT and U that GOSAT would see at the SGP site, using the
479 GOSAT averaging kernels and priors. The measurement error and
480 interference terms are assumed to be zero for this analysis.

481
482 Using this analysis, the importance of the prior is assessed by using either a
483 prior that is constant in location and time (with only a 2 ppm/year secular
484 increase) or the GOSAT prior, in Eqs. 5 and 6. We assess how much LMT
485 and U contribute to the variations seen in XCO₂ using the variability of the
486 LMT and U partial columns combined with the weighting each has in the full
487 column. The seasonal cycles of each partial column mixing ratio are studied
488 by adjusting all aircraft measurements at SGP (2009 to 2014) to common
489 year (2012) by applying a 2 ppm/year secular trend, and binning all
490 observations by month. This method was used rather than fitting the
491 aircraft observations using the NOAA fitting routine (CCGCRV, described in
492 Thoning et al., 1989) to estimate the seasonal cycle shape because we found
493 that the aircraft observations (matched to GOSAT and within the GOSAT
494 record) are not sufficiently smooth to result in a consistent fit. Figure 4
495 shows the estimates of LMT, U, and XCO₂ using SGP aircraft profiles
496 calculated as described above. There is significant variability in the
497 individual aircraft measurements, seen in panel (a) but this is smoothed out
498 on monthly timescales, seen in the remaining panels. The dashed lines in
499 panel a represent fits using the NOAA fitting software CCGCRV. Single U
500 partial column mixing ratios are rarely more than 1 ppm different from the
501 fit, whereas single LMT mixing ratios can be up to 5 ppm different (e.g. see
502 summer, 2009; January, 2010; Summer, 2011).

503
504 Figure 4 (b) and (c) show the difference between the simulated retrievals
505 with the GOSAT a priori (b) versus a flat a priori (c) for the seasonal cycle.
506 The patterns are very similar, indicating that the signal is primarily coming
507 from the data rather than the prior, with standard deviations of 0.8 ppm for
508 LMT and 0.3 ppm for U (these changes are fully characterized when applying
509 the GOSAT prior to the aircraft true profile with the specified a priori vector).

510
511 Figure 4, panel (d) shows U versus XCO₂. At first glance U and XCO₂ look
512 very similar, but by comparing panel (d) and (b), the XCO₂ deviations move
513 towards LMT relative to the prior. The seasonal variabilities of XCO₂, LMT,
514 and U (maximum minus minimum), are 3.3 ppm, 4.8 ppm, and 3.3 ppm,
515 respectively. Note that the seasonal variations in LMT and U have a 0.56
516 correlation suggesting some independence between these two variables. A

517 straightforward calculation of variation times airfraction (Eq. 4) show that
518 the fraction of variation of XCO₂ resulting from variations in LMT is
519 approximately 30%, and the fraction of the variation in XCO₂ coming from U
520 variation is roughly 70%. It is expected that U has the much larger impact
521 on XCO₂ due to the fact that the full column is 77% LMT. A similar
522 calculation at Park Falls, where the LMT seasonal cycle is 20 ppm and the U
523 seasonal cycle is 5 ppm finds 45% of the seasonal variability in XCO₂ results
524 from U and 55% from LMT at Park Falls (46N). Here, the high variability in
525 LMT will have a much large impact on XCO₂ despite the fact that it
526 represents a smaller part of the column.

527
528 Figure 4 indicates that LMT and U do have unique seasonal cycles which
529 result from the data rather than the prior. The LMT partial column, which
530 contributes to 30% of the variations observed in XCO₂, has a much larger
531 seasonal variability than the U partial column or the XCO₂ column, and
532 earlier seasonal cycle maximums and minimums.

533

534 **4.0 Methods**

535 We test the sensitivity of the new products to surface fluxes using back-
536 trajectory footprints in Section 4.1. Section 4.2 discusses how GOSAT is
537 compared to aircraft. Sections 4.3-4.5 describe the bias correction, how the
538 aircraft data is extended to the full atmosphere and the coincidence criteria.

539

540 **4.1 Sensitivity of the LMT and U partial column mixing ratios to** 541 **surface fluxes**

542 To compare LMT and U sensitivity to surface fluxes, we look at 10-day back-
543 trajectory footprints created using Weather Research and Forecasting (WRF)
544 model combined with the Stochastic Time-Inverted Lagrangian Transport
545 (STILT) model (WRF-STILT; Nehrkorn et al., 2010). The "footprint" for an
546 observation is a map of the surface locations to which an observation is
547 sensitive. Footprints are created for each of the 20 GOSAT levels, then
548 convolved with the LMT and U averaging kernels. The averaging kernel
549 estimates the sensitivity of the GOSAT measurement of each quantity to the
550 true state at each level. Footprint maps are created which show the
551 sensitivity of each type of GOSAT observation to sources and sinks. This
552 was done for 10 GOSAT observations in the Amazon. The average distance
553 for the nearest 10% of footprints is 260 km for LMT and 790 km for U. It is
554 likely that there is also a very long tail in the U sensitivity, based on the
555 work of Liu et al. (2015) and Feng et al. (2016).

556

557 **4.2 Comparisons to aircraft**

558 The correct way to validate GOSAT estimates of [LMT, U] is to compare the
559 GOSAT observations to an estimate of what GOSAT should observe, given its
560 sensitivity, when the true atmospheric state is set to the aircraft CO₂ profile

561 using Eq. 6. The agreement should be within the GOSAT observation error,
562 as the smoothing term's effects on the comparison are removed by the
563 application of the GOSAT averaging kernel to the validation data. The
564 aircraft measurements are assumed to be unbiased and have small
565 measurement error compared to the errors in the GOSAT profiles.

566

567 **4.3 GOSAT bias correction**

568 The GOSAT standard XCO₂ product has regional biases and errors which can
569 be partially corrected using jointly retrieved parameters, pre-filters, or
570 radiance properties, e.g. the ratio of the signal in the strong vs. weak band,
571 retrieved albedo slopes or values, retrieved aerosol slopes or values; and
572 through post-processing screening, e.g. removing fits where the difference
573 in the retrieved versus prior surface pressure is greater than 4 hPa. We
574 apply the same techniques to the LMT partial column mixing ratio in
575 Appendix A which is briefly described here. After LMT is corrected, the
576 corrected U partial column mixing ratio is set using Eq. 9a, so that XCO₂ is
577 consistent with LMT and U. The purpose of setting U this way is a) there is a
578 lack of validation data for the U partial column, so bias correction would be a
579 lot less certain, and b) it is useful to have the new products consistent with a
580 current operational column results.

581

582 To correct the LMT partial column mixing ratio, a set of pairs of "true" and
583 "retrieved" values is compiled, using validation data. GOSAT minus true is
584 plotted versus various GOSAT parameters described in Appendix A, and if a
585 slope is found for the GOSAT error versus any parameter, then a correction
586 is applied for that parameter. The robustness of the correction is tested by
587 verifying the correction on data withheld from the fit, as described in
588 Appendix A. Following the initial bias correction, GOSAT LMT is compared for
589 closely occurring ocean and land pairs; a constant bias term is added to the
590 land bias correction so that land and ocean, on average, are consistent.

591

592 **4.4 Coincidence criteria**

593 "Geometric criteria", defined as +/-3 degrees latitude, +/-5 degrees longitude
594 +/-1 week time are used to select coincident GOSAT observations for
595 particular sites. 5 degrees latitude/longitude, 1 hour has previously been
596 used for GOSAT criteria (Kulawik et al., 2016), however this did not yield
597 enough matches for aircraft profiles. With the above criteria, the total
598 matches range from 64 (at Poker Flats, station ID PFA) to 4800 (at the
599 Southern Great Plains, station ID SGP), with median 430, which is
600 approximately 9/month assuming all months are equally well sampled
601 throughout the time series. A tight spatial criteria was selected to best
602 capture the seasonal cycle at a given location, especially for land where
603 spatial variability is large. Because aircraft and surface observations are
604 more infrequent than TCCON, an extended temporal window was used for

605 the comparisons to obtain sufficient comparison data. Other methods that
606 were tried were dynamic coincidence criteria (Wunch et al., 2011b) which
607 considers a larger area (+- 10 degrees latitude, +- 30 degrees longitude)
608 but also matches atmospheric temperature, and a variant of Basu criteria
609 (Guerlet et al., 2013), which used dynamic coincidences which had model-
610 model differences less than 0.5 ppm. All three criteria gave similar results
611 overall, with different criteria performing better at different stations, but no
612 clear overall best criteria. For HIPPO data, which mainly tests latitude
613 gradients over ocean, the dynamic coincidence approach was used following
614 Frankenberg et al. (2016). Different variations on the dynamic coincidence
615 criteria were tested, e.g. using temperature comparisons at the surface,
616 averaging from the surface to 2.5 km, or weighting temperature differences
617 by the pressure weighting function. The different temperature criteria
618 yielded similar results overall, other than using temperature differences at
619 the surface did not work as well as the other levels. We therefore used the
620 standard dynamic criteria from Wunch et al., (2011b).

621

622 **4.5 Extension of the aircraft profile**

623 The aircraft measurements go from the surface to between 5.5 km to 8 km
624 for most ESRL land to 9-13 km for HIPPO observations. As GOSAT LMT, U,
625 and XCO₂ have sensitivity above 5.5 km and even above 13 km, as seen in
626 the averaging kernel shown in Fig. 3, the aircraft profile needs to be
627 extended from the top measurement to the top of the atmosphere. Four
628 different methods of extension were tested: extending with the GOSAT
629 prior, extending the top aircraft measurement through the tropopause
630 pressure and extending with the GOSAT prior above this, extending with the
631 CT2015 model, and extending the top aircraft measurement through the
632 tropopause pressure and extending with the CT2015 model above this. The
633 different extensions mainly had an effect on the overall LMT, U, and XCO₂
634 biases, rather than the standard deviation, with a spread of 0.4 ppm, as
635 seen in Table A4. The extension that was used in the rest of the paper is
636 extending the top aircraft measurement through the tropopause pressure
637 and extending with the CT2015 model above this. There was no clear
638 winner on the profile extension, and this choice was just a preference.

639

640 **5. GOSAT results**

641 Figure 5 shows GOSAT comparisons for LMT and U versus the aircraft
642 measurements at the SGP site at 37N, 95W which can be compared to the
643 simulated results shown in Fig. 4. The GOSAT LMT and U products show the
644 same seasonal patterns as seen in the aircraft data. Figure 5a shows results
645 without bias correction (though do apply a constant 12 ppm correction to
646 LMT). The GOSAT results show a similar seasonal cycle to the aircraft but
647 with large and temporally correlated errors. Figure 5b shows the results
648 with the bias correction as described in Appendix A. Figure 5c shows

649 CarbonTracker matched to GOSAT (CT@GOSAT) and CarbonTracker
650 matched to the aircraft measurements (CT@aircraft). The difference of
651 CT@GOSAT and CT@aircraft estimates the co-location error. Large
652 differences are seen between CT@GOSAT and CT@aircraft in early 2010,
653 Summer, 2010, and Summer, 2011. In Fig. 5d, the seasonal cycle is shown
654 by transforming all data to lie within 2012 using 2 ppm/year adjustment to
655 CO₂. There are systematic differences seen in the drawdown, which is
656 underestimated by GOSAT. However, when months that have differences of
657 (CT@GOSAT -CT@aircraft) more than 2.5 ppm are removed (removing June,
658 2009; October, 2009; May, 2010; July, 2010; and August, 2010), Figure 5e
659 shows agreement within the GOSAT predicted errors between GOSAT and
660 aircraft. Figure 5f is the same as Figure 5e, but removes all observations
661 that were used to develop the bias correction. There is no significant
662 difference between Fig. 5f and 5e. The authors have some concerns about
663 applying the bias correction to parts of the world where there is not
664 validation data, e.g. the land bias correction was primarily over the U.S..
665 Similarly, the HIPPO observations used for ocean bias correction are in the
666 Pacific Ocean, so the ocean bias correction in the Atlantic Ocean is less
667 certain.

668
669 GOSAT U improves over the a priori for actual observations (Figs. 5d-f) and
670 in simulated (Fig. 4b) results. This is shown by the black (aircraft) vs. blue
671 (GOSAT) in Fig. 5c where there is better agreement in July-November than
672 prior (green) vs. black (aircraft). The bias seen in the U partial column
673 mixing ratio versus the aircraft U estimate is also found in XCO₂ versus the
674 aircraft.

675

676 **5.1 Summary of comparisons to all validation data**

677 GOSAT LMT, U, and XCO₂ are compared to aircraft profiles, where the
678 aircraft profile has the GOSAT averaging kernel applied so that the
679 sensitivity is considered. The comparison locations are shown in Fig. 2.
680 More detailed comparisons, showing results for each location and/or
681 campaign, are shown in Appendix B. Definitions of the quantities calculated
682 and compared are shown in Table 3.

683

684 Table 4 shows the biases with respect to aircraft data and Table 5 shows the
685 standard deviation with respect to aircraft, for single and averaged
686 observations. The bias or standard deviation is calculated for every site (or
687 campaign). The mean represents the average of all site means, and the ±
688 represents the standard deviation for the means averaged by site (or
689 campaign). The variability of the bias by location or time is a key metric in
690 the data quality. Biases that vary by season or location are cannot be
691 corrected for and will be particularly detrimental to the use of satellite data

692 for inverse flux estimates, as the assimilation will attribute these biases to
693 spurious fluxes.

694
695 The co-location error is estimated by comparing CarbonTracker to itself at
696 the satellite location/time and CarbonTracker at the aircraft location/time.
697 For the ocean surface sites, a vertical co-location error is estimated by
698 comparing CarbonTracker with the LMT averaging kernel to CarbonTracker
699 at the surface. In Tables 4-6, the top entry in the ocean surface co-location
700 error is from discrepancies in horizontal location and time. The bottom entry
701 is the co-location error for sampling CarbonTracker for the LMT quantity
702 versus CarbonTracker at the surface.

703 704 **5.1.1 Bias**

705 In Table 3, the co-location bias is largest for aircraft land, with an overall
706 bias of -0.6 ppm and bias variability of 0.7 ppm. This gives an approximate
707 best case of what could be achieved by GOSAT-aircraft comparisons. An
708 investigation of the -2 ppm co-location bias in the LMT partial column mixing
709 ratio at CAR in July (during the drawdown) finds that the GOSAT
710 observations are always taken 3-4 hours later than the aircraft. The
711 CarbonTracker model estimates the effect of +3 hours as resulting in a -2
712 ppm change in the LMT partial column mixing ratio. The co-location bias
713 reflects spatial, diurnal, and seasonal co-location errors. Taking out the 5
714 sites that have co-location biases > 0.5 ppm (see Appendix B, Table B1:
715 WBI, BNE, CAR, HIL, and CMA), reduces the co-location bias to -0.2 ± 0.3
716 ppm.

717
718 In Table 4, the "true mean by site/campaign" is the mean true value
719 averaged by location (or campaign). The \pm represents the standard
720 deviation of the mean true value by location (or campaign). The GOSAT
721 retrieval must improve on the \pm at the very least to provide information on
722 the atmospheric state. The GOSAT prior bias improves over the true
723 variability on land but not for ocean cases for LMT. For U, the a priori minus
724 true variability is the same size as the true variability. The "GOSAT bias"
725 improves over the prior in all entries of the absolute bias, except for XCO₂
726 for ESRL ocean, and U and XCO₂ for AJAX. Issues with both U and XCO₂
727 suggests a possible issue with the profile extension above the aircraft.
728 Improvement over the prior for GOSAT \pm bias occurs in all comparisons.
729 Note that for ESRL land, if the 5 stations with large co-location error are
730 taken out, the LMT bias variability decreases from 1.0 ppm to 0.7 ppm.

731
732 The location-dependent bias is important because this bias variability cannot
733 be easily corrected and will be attributed to phantom fluxes. The LMT
734 location dependent bias is no worse than the XCO₂ location dependent bias,
735 whereas the LMT signals are much more variable than XCO₂. The bias

736 variability for XCO₂ and U are possibly too high due to uncertainty of the
737 aircraft profile extension because the bias variability is much larger than the
738 0.3 ppm seen in Kulawik et al. (2016) versus TCCON. Taking out sites with
739 large co-location bias for XCO₂ does not improve the GOSAT XCO₂ bias
740 variability. Taking out the top 4 GOSAT XCO₂ bias outliers results in a
741 GOSAT XCO₂ bias variability of 0.5 ppm for the remaining sites, however
742 these 4 sites are not the same sites where LMT has bias issues, nor are
743 these sites where CarbonTracker shows a large co-location bias.

744

745 **5.1.2 Standard deviation**

746 Table 5 calculates errors versus aircraft data. The co-location error gives an
747 upper bound on how well we could expect GOSAT to compare to the
748 observations. The co-location error is subtracted, in quadrature, from the
749 GOSAT error to estimate the GOSAT errors in the absence of co-location
750 error.

751

752 To reduce the co-location error, a very tight coincidence criteria of 2
753 degrees, 1 hour was applied, yielding 146 matches, of which 89 are at SGP
754 and 39 at HIL. Results for these tight coincidences are compared to the
755 looser coincidence criteria results for these sites. For the tighter
756 coincidences, the LMT co-location error is (0.3,0.7) ppm at (SGP, HIL,
757 respectively), and the GOSAT LMT (n=1) error is (2.6,2.5) ppm. This is
758 compared to the looser coincidence results, where LMT co-location error is
759 (1.8,2.2) ppm and GOSAT LMT error is (3.9,3.8) ppm. This analysis
760 suggests that the co-location error based on CarbonTracker may be
761 underestimated. The GOSAT LMT (n=1) error in Table 5 for ESRL land
762 (which has co-location error subtracted) is 3.4 ppm, whereas the error when
763 the tighter coincidence criteria is applied is actually much less, 2.6 ppm. For
764 U, the GOSAT (n=1) error is (1.0,1.4) whereas it is (1.3,1.2) for the looser
765 criteria, so tight versus loose coincidence criteria did not matter a lot for U
766 comparisons.

767

768 The next row of Table 5 is the predicted error, given by Eqs. 7 and 9, which
769 is on the order of 4.5 ppm for LMT, 1.7 ppm for U, and 0.7 ppm for XCO₂.
770 The actual standard deviation of GOSAT versus aircraft, however, is about
771 half that for LMT and U, and double the predicted error for XCO₂. This is
772 discussed in Section 5.1.5.

773

774 The "true variability" in Table 5 shows how much the different partial
775 column mixing ratios vary by month. The variability of LMT over land is 5.4
776 ppm, about double that of U or XCO₂, and the variability of LMT at remote
777 ocean sites is 1.1 ppm, about 50% larger than U or XCO₂ variability.

778

779 The prior standard deviation ($n=15$), and GOSAT standard deviation ($n=15$)
 780 look at the error of averaged GOSAT values, which is important for
 781 understanding bias that will result from assimilating this data for flux
 782 estimates. Kulawik et al. (2016) showed the GOSAT error does not drop off
 783 as the inverse square root of the number of observations, like it would if the
 784 error were fully random. The error for 15 observation averages is about 0.4
 785 times that of 1 observation for land, with a similar factor for XCO₂, LMT, and
 786 U; and about 0.5 times that of 1 observation for ocean, similarly for all
 787 quantities. Note that the co-location error has been subtracted out (in
 788 quadrature) for both the a priori and GOSAT errors.

790 The standard deviations for LMT, U, and XCO₂ show improvement over the
 791 prior for land cases but improve only marginally or do not improve over
 792 ocean. The location-dependent bias, however, does show improvement for
 793 LMT and U in Table 4. For surface ocean sites, which are only compared to
 794 LMT, the improvement over the prior is much better, mainly because the
 795 prior is not very good at these sites.

796 **5.1.3 Errors separated into co-location, random, and correlated error**

797 The errors between aircraft and GOSAT observations can be parametrized by
 798 the number of GOSAT observations that are averaged. Kulawik et al. (2016)
 799 found the form in Eq. 11 matched well to the observed errors.

$$801 \quad \text{error} = \sqrt{a^2 + b^2/n} \quad (11)$$

$$802 \quad \text{error} = \sqrt{\varepsilon_{coloc}^2 + a_o^2 + b^2/n} \quad (12)$$

803 where n are the number of GOSAT observations that are averaged (all of the
 804 averaged observations match a single aircraft measurement), a is error that
 805 does not reduce with averaging, and b is the random error. a is further split
 806 into co-location error, ε_{coloc} , plus a_o , the correlated error in Eq. 12. Correlated
 807 error means that no matter how many observations are taken, this error
 808 does not reduce, and can be due to interferences or spectroscopy in
 809 combination with attributes specific to different locations and times.

810 The co-location error is the error resulting from imperfect matching of the
 811 aircraft and satellite observations, and is approximated by the standard
 812 deviation of the CarbonTracker model at the validation location and time and
 813 the model at the satellite observation location and time, and is tabulated in
 814 Table 6. This term, as seen in Table 6, is comparable to or even larger than
 815 a for LMT land cases. Some co-location schemes (e.g. as implemented by S.
 816 Basu described in Guerlet et al. (2013)) use the model-model differences to
 817 select the best satellite observations to match validation data. Equation 11
 818 is used to determine a and b , and then a_o is calculated from a and ε_{coloc} .

822
823 The co-location error is subtracted from the correlated error, to try to
824 remove the effect of co-location on the error estimate. This is a statistical
825 subtraction, as no value was found in subtracting the co-location error for
826 individual comparisons (perhaps because the model is not accurate enough
827 to capture the co-location differences case by case). The three quantities
828 from Eq. 12 are shown in Table 6. For LMT the co-location error is about the
829 same size as the correlated error for ocean, and the co-location error is
830 larger than correlated error for land. For U and XCO₂, the correlated errors
831 are larger than the co-location error for ocean, and comparable for land.

832

833 **5.1.4 Comparison of XCO₂ results to previous results**

834 We compare GOSAT XCO₂ comparisons to the previous validations using
835 TCCON (Wunch et al., 2011b; Kulawik et al., 2016) and HIPPO observations
836 (Frankenberg et al., 2016). The GOSAT comparisons to HIPPO in
837 Frankenberg et al. (2016) were for at least 6 averages and did not subtract
838 co-location error (which is only 0.1 ppm over ocean). Using Eq. 12 and
839 Table 6, we find that the XCO₂ error for n=6 is 0.43 ppm, in agreement with
840 0.45 from Frankenberg et al. (2016). Without co-location error, the XCO₂
841 from n=6 is 0.42 ppm. For ESRL land, several quantities in Tables 4-6 can
842 be directly compared to previous GOSAT/TCCON validation: the co-location
843 error (0.8 ppm) is larger than co-location for geometric coincidence (0.4
844 ppm) but smaller than for dynamic coincidence (0.9 ppm) from Kulawik et
845 al. (2016). This makes sense as Kulawik et al. (2016) had a 1 hour
846 coincidence with TCCON whereas 7 days is used in this paper (because
847 aircraft measurements are sparser in time than TCCON observations). a_o
848 and b values of 0.7±0.5 ppm and 1.6±0.2 ppm in this work are consistent
849 with 0.8 ±0.2 ppm and 1.6±0.1 ppm, for a (corrected) and b, respectively,
850 from Kulawik et al. (2016) Table 2. Additionally, the predicted error of
851 0.9±0.1 which is a factor of 1.9 less than the actual error of 1.7±0.4 are
852 identical to the values and relative sizes of predicted versus actual error in
853 Kulawik et al. (2016) at the end of section 3.1.

854

855 As discussed in Section 5.1.1, the location-dependent bias found in Kulawik
856 et al. (2016) versus TCCON sites for XCO₂ was 0.3 (after removing outlying
857 stations north of 60N and locally-influenced stations). In this paper, we find
858 the bias variability for XCO₂ 0.9 ppm over land and 0.3 ppm over ocean (see
859 Table 4). One reason for the discrepancy could be from the extension of the
860 profile above the aircraft measurement (about 5-6 km). As seen in
861 Appendix A, different methods for profile extension causes changes on the
862 order of 0.4 ppm. Another possible cause for the discrepancy is that GOSAT
863 has been extensively tested against TCCON and issues that show up at
864 TCCON locations have been previously addressed. This was tested by fitting
865 bias correction factor for U specifically, rather than calculating bias-

866 correction factors for LMT and subtracting the LMT partial column from
867 GOSAT XCO₂ to estimate U. The bias variability for U did not improve when
868 bias correction factors were calculated directly for U. We also compare
869 GOSAT XCO₂ comparisons aircraft and GOSAT XCO₂ comparisons to TCCON
870 at the two sites where both validation data are co-located, Park Falls,
871 Wisconsin (LEF), and Lamont, Oklahoma (SGP). Note that LEF and SGP
872 collect data up to 3.5 and 5 km above the ground, respectively, whereas
873 most sites collect up to 8 km above the ground, so the profile extension
874 error might be higher at these sites. Averaging over these two sites, the
875 GOSAT XCO₂ bias versus aircraft in this work is -0.4 ppm. The GOSAT XCO₂
876 bias versus TCCON in Kulawik et al. (2016) for these two sites is -0.1 ppm.
877 The difference between these comparisons is on the same order as the
878 uncertainty introduced by profile extension discussed in Appendix A.

879

880 **5.1.5 Predicted and actual error correlations**

881 One surprising finding is that LMT and U actual errors are less than the
882 predicted errors whereas the actual XCO₂ errors are larger than predicted,
883 even though all three errors are calculated from the same error covariance
884 (see Eqs. 7-8). Equation 9c relates the errors in LMT, U, and XCO₂. For
885 land, an XCO₂ error of 0.9 ppm is consistent with an LMT error of 4.6 ppm, U
886 error of 1.8 ppm, and error correlation of -0.8. The XCO₂ actual error (1.7
887 ppm) is much *larger* than the predicted error whereas the LMT and U errors
888 are *smaller* than predicted.

889

890 The discrepancy between the actual and predicted errors arises from the
891 actual correlation of the LMT and U partial column mixing ratio errors. The
892 predicted error correlation between LMT and U is -0.8. This means that
893 values too low in LMT should be matched with values too high in U, such
894 that the total column has lower relative errors than either partial column
895 separately. The actual error correlation of (LMT-aircraft) and (U-aircraft)
896 averages +0.6, meaning that when LMT is high, U also tends to be high, and
897 XCO₂ does not gain precision when combining LMT and U. So the finding is
898 that the LMT-U error correlation must be changed from the predicted value
899 of -0.8 to the measured value of +0.6. When the diagonal error terms are
900 multiplied by 0.6 and the error correlation between LMT and U is set to 0.6,
901 to match the error correlations observed versus aircraft data, the predicted
902 LMT, U, and XCO₂ errors are consistent with the actual errors. Over ocean,
903 multiplying the diagonal error terms by 0.3 and the error correlation
904 between LMT and U set to 0.6 makes the predicted and actual errors agree.

905

906 The errors in Table 5 represent the standard deviation of GOSAT minus
907 validation data calculated separately at each validation location. So, the
908 errors in Table 5 do not include the bias errors from Table 4. The persistent
909 regional biases captured in the "GOSAT bias" variability also reflect errors in

910 the GOSAT measurement and should somehow be combined into the full
911 error. These regional biases likely result from persistent interferent errors,
912 such as due to aerosols, or an interaction between spectroscopic errors and
913 local conditions. Some but not all of the bias, particularly for LMT land, can
914 be attributed to co-location error (see Table 4). The correlation of the LMT
915 and U location-dependent biases (using biases separated by location from
916 Table B1) is also positive, 0.6, similar to the correlation of the individual
917 errors in LMT and U, so this would not account for the discrepancy between
918 the predicted correlation of -0.8 and actual correlation of 0.6 between the
919 LMT and U errors. Another possible reason for the positive error correlation
920 in LMT and U is that it is a consequence of the bias correction. The error
921 correlation on the uncorrected data was found to be -0.8, which supports
922 that the bias correction modifies the error correlation between U and LMT.
923 This is the first characterization of the effect of bias correction on the actual
924 errors.

925
926 In summary, the single-sounding errors of GOSAT LMT and U over land
927 (ocean), based on the ESRL aircraft comparison, and subtracting co-location
928 error, are 3.4 and 1.3 ppm (1.5 and 0.8 ppm) respectively, with a positive
929 correlation of 0.6. This is consistent with the XCO₂ error of 1.8 (1.0) ppm
930 for land (ocean), using Eq. 9c. To find the error of averaged LMT and U, the
931 single-sounding errors can be replaced by Eq 11, with *a* and *b* values given
932 in Table 6, and the same LMT-U error correlation of 0.6.

933
934 **5.2 Variability within the U.S.**
935 The CarbonTracker model identifies 19 eco-regions within North America
936 (http://www.esrl.noaa.gov/gmd/ccgg/carbontracker/CT2011_o/documentati
937 [on_assim.html](http://www.esrl.noaa.gov/gmd/ccgg/carbontracker/CT2011_o/documentati)). The ESRL aircraft stations can be broadly grouped into
938 conifer forest: PFA, ETL, ESP, THD; grass/shrub: CAR, BNE; crops: HIL,
939 WBI, SGP; forest/field: DND, LEF, NHA, CMA, SCA; and mixed: TGC. The
940 variability at these sites is a combination of the local activity at the site,
941 latitude of the site, and transport into/out of the site.

942
943 Maps of GOSAT LMT, U, and XCO₂ along with aircraft, surface, tower, and
944 TCCON observations for February and July are shown in Fig. 6 (converted to
945 2012 by subtracting 2 ppm per year secular increase). In February, the
946 lower troposphere has already reached near peak values, whereas the U
947 partial column is continuing to increase through April. In July, there is a
948 large gradient in the LMT, primarily west to east, but also north to south,
949 seen also in the stations shown in Fig. 6. The LMT pattern agrees with
950 aircraft (Sweeney et al., 2015) and tower patterns, showing that GOSAT
951 LMT is able to see variations in the summertime CO₂ depletion near the
952 surface due to biospheric processes. The U partial column shows more
953 discrepancies with aircraft than LMT which is in general agreement, and the

954 same pattern of discrepancies are also seen for XCO₂ versus aircraft. At the
955 two sites where aircraft and TCCON are jointly observed, SGP in Oklahoma
956 and LEF in Wisconsin, XCO₂ agrees with TCCON rather than the aircraft.
957 This suggests an issue with the extension of the aircraft profile from the top
958 aircraft measurement (about 6 km) to the top of the atmosphere.

959
960 Figure 7 shows the seasonal cycle at 5 sites arranged west-to-east (a-e) and
961 north-to-south (f-j). The seasonal cycle amplitude in LMT increases for both
962 west-to-east and south-to-north directions. There is also a shift to later in
963 the seasonal cycle minimum going either east to west and north to south, as
964 seen by the slopes in the orange and blue dotted lines. There is a consistent
965 phase lag in the U-prior which is corrected by the GOSAT retrieval, and the
966 LMT prior drawdown is consistently too large in panels i and j, correct for the
967 GOSAT retrieval. The seasonal cycle maximum is harder to quantify for the
968 LMT because LMT CO₂ rises and stays fairly flat between January and April,
969 therefore the maximum can be influenced by small variations in the data, in
970 contrast to U or XCO₂ which rise steadily until April.

971

972 **5.3 Comparisons to remote surface ocean sites**

973 Remote surface sites are useful as comparisons to LMT as these locations
974 are expected to have long vertical length scales of variability near the
975 surface. These comparisons LMT and remote surface ocean sites are not
976 used for estimating errors or bias corrections because there is a mismatch in
977 sampled vertical air mass: to compare validation data and GOSAT LMT
978 properly, validation values are needed at every pressure level at which the
979 GOSAT LMT averaging kernel (as seen in Fig. 3) is not zero. Since there is
980 only validation data at the surface, the only option is to directly compare the
981 surface site value to the GOSAT LMT result, rather than integrating
982 validation results over the pressure range where GOSAT LMT is sensitive.
983 The vertical co-location error is estimated by comparing CarbonTracker LMT
984 (estimated with Eq 6b, where \mathbf{x}_{true} is set to the CarbonTracker value, \mathbf{x}_a
985 is the GOSAT prior, and cross-state error and measurement error are set to
986 zero) versus CarbonTracker surface values. The GOSAT LMT a priori is
987 significantly worse for remote ocean sites as compared to North America,
988 and this allows the GOSAT product to show what is in the data versus the
989 prior. In Table 6, the co-location error for surface ocean sites is higher than
990 for ocean aircraft comparisons (1.0 ppm vs. 0.3 ppm, respectively), and the
991 GOSAT bias versus ocean surface sites in Table 4 is also higher (1.1 ppm vs.
992 0.1 ppm, respectively). Because of the limited GOSAT ocean coverage,
993 there are typically only about 4 consecutive months for each station, but this
994 is adequate to evaluate the performance. Figure 8 shows an average over
995 all locations, and the 4 sites with the highest number of matches, arranged
996 from north to south. Note the improvement of GOSAT (red) over the a priori
997 (green) when comparing to the surface site measurements (pink).

998 Unsurprisingly, the performance of XCO₂ (blue) shows that surface site
999 observations are not suitable for XCO₂ validation. GOSAT LMT improves
1000 over the prior in terms of the overall bias, the bias variability, and the
1001 standard deviation over the prior even without averaging; the error reduces
1002 further with averaging.

1003 Table 6. Estimated co-location, correlated, and random errors using Eq. 12.
1004 The co-location errors are taken from Table 4.

1005

1006 **5.4 Source versus outflow in biomass burning with comparisons to** 1007 **MOPITT CO and MODIS fire counts**

1008 The SH region is of particular interest for validation as the GOSAT prior is
1009 nearly spatially and vertically constant, varying primarily by month. Figures
1010 9 and 10 compare GOSAT LMT and U partial column mixing ratios,
1011 respectively, to MOPITT multispectral CO retrievals and MODIS fire counts,
1012 to see how much fires in this part of the world are responsible for the
1013 patterns seen in the GOSAT partial columns. The GOSAT prior, in the left
1014 columns of Figs. 9 and 10, is nearly constant in the southern hemisphere.
1015 The scale needed to span the seasonal range is about 13 ppm, about half
1016 that needed to capture the seasonal variability in the U.S.

1017

1018 The pattern seen in LMT matches MODIS fire count images, shown in the
1019 right column, and matches MOPITT near-surface CO shown in the third
1020 column. Because of the different overpass time and the different coverage
1021 due to cloudiness between these satellites, an exact match should not be
1022 expected. In February, sub-Saharan Africa has fires and south-central Africa
1023 does not, whereas the situation is reversed in August. This pattern is seen
1024 in GOSAT LMT, MOPITT near-surface, and MODIS fire counts. The main
1025 differences between GOSAT and MOPITT are seen in October, where GOSAT
1026 LMT shows outflow over the Atlantic and MOPITT near-surface CO does not.
1027 This may be because the multi-spectral CO has little surface sensitivity over
1028 the ocean.

1029

1030 In the mid-troposphere, MOPITT CO shows enhancement in sub-Saharan
1031 Africa in February, central Africa in August, and outflow in October, and
1032 GOSAT retrieved U shows the same patterns as MOPITT. Interestingly, both
1033 MOPITT and GOSAT show no enhancement in South America in August,
1034 whereas the surface shows very strong enhancements in both. MOPITT
1035 shows very little outflow in September, but strong outflow in October.
1036 GOSAT does not have ocean coverage in this region for September, but
1037 GOSAT U shows strong outflow in October.

1038

1039 The LMT signal in the Amazon region is clearly visible by May (not shown),
1040 whereas the CO signal seen from MOPITT

1041 (http://www.acom.ucar.edu/mopitt/MOPITT/data/plots6j/maps_mon.html)

1042 seems to ramp up starting in August. We look at the quantitative values for
1043 the enhancements and background values for surface CO and LMT CO₂ in
1044 Table 7 and use this to estimate ΔCO/ΔCO₂ emission ratios for May and
1045 August.

1046
1047 The GOSAT LMT degrees of freedom are about 0.8 and do not vary
1048 significantly, mainly because only clear-sky observations (with
1049 aerosols/clouds < 0.3 optical depth) are used. The MOPITT degrees of
1050 freedom for the near-surface varies significantly. MOPITT enhancement for
1051 different degrees of freedom cutoffs are shown in different columns of Table
1052 7. To account for the degrees of freedom, note that if a retrieved variable
1053 has degrees of freedom 0.2, it will capture about 20% of the true variability;
1054 if a retrieved variable has degrees of freedom 0.4, it will capture about 40%
1055 of the true variability. So, an estimate of the emission ratio which considers
1056 the degrees of freedom is:

$$1057 \text{emission ratio} = \frac{CO - \text{background (ppb)}}{CO_2 - C_2 \text{ background (ppb)}} * \frac{CO_2 \text{ degrees of freedom}}{CO \text{ degrees of freedom}} \quad (13)$$

1058
1059 Without utilizing a model as a transfer function, the exact ratio cannot be
1060 estimated, due to the varying sensitivities with altitude and different
1061 observation locations and times.
1062

1063
1064 The emission ratio is estimated using Eq. 13 with the information shown in
1065 Table 7. The emission ratio estimate ranges from 6-7% in May and 10-15%
1066 in August, for the different MOPITT sensitivity groupings. The emission ratio
1067 seen by the MOPITT and GOSAT LMT products are compared to those
1068 estimated from aircraft observations over tropical forests by Akagi et al.
1069 (2011, Table 1), which is 8.8%. The MOPITT/GOSAT ratio is similar to Akagi
1070 et al. (2011), but 2-3% lower in May, and 1-6% higher in August.

1071 1072 **5.5 Differences between LMT and U**

1073 The difference between CO₂ in the free troposphere and boundary layer can
1074 be used to evaluate model transport. One previous finding is that surface
1075 assimilation estimates of northern extra-tropical and southern hemisphere
1076 land flux differences are correlated with the gradients between CO₂ at 4 km
1077 and 1 km in the assimilated model. When the model-based vertical
1078 gradients of CO₂ are larger than aircraft observations, models tend to predict
1079 too large northern hemisphere sinks and too large southern hemisphere
1080 sources (Stephens et al., 2007). Aircraft observations of CO₂ at 4 km and 1
1081 km are taken at only a few sites worldwide, primarily in the U.S. Therefore,
1082 global measurements of the difference between CO₂ in the free troposphere
1083 and boundary layer are of great interest. In this section we calculate the
1084 errors for LMT-U compared to aircraft profiles and show this difference for

1085 GOSAT and CarbonTracker in the U.S. and the southern hemisphere in two
1086 different months.

1087
1088 The error estimate for LMT-U is calculated using Eq. 14. Note that a positive
1089 correlation in the errors for LMT and U results in a smaller error for the
1090 quantity (LMT – U) than the sum of the squares of LMT and U.

1091
1092
$$\sigma_{(LMT-U)} = \sqrt{\sigma_{lmt}^2 + \sigma_u^2 - 2 \cdot \sigma_{lmt}\sigma_u c} \quad (14)$$

1093
1094 Table 8a-c give the bias, standard deviation, and error with averaging for
1095 LMT – U. In Table 8a, the GOSAT bias and bias variability of (LMT – U)
1096 improves over the prior for all cases. The bias variability of 0.3, 0.9 and 0.8
1097 ppm of (LMT – U) for HIPPO ocean, ESRL ocean, and ESRL land,
1098 respectively, is comparable to the LMT bias variability of 0.3, 1.0, and 1.0 for
1099 the same categories. In Table 8b, the 15-observation average standard
1100 deviation for GOSAT LMT-U is 0.6 (1.2) ppm for ocean (land), 0.2 ppm
1101 higher for ocean and 0.7 ppm lower for land than LMT. In Table 8c, the
1102 correlated error is 0.5 (0.9) ppm for ocean (land), which is 0.2 ppm higher
1103 for ocean and 0.8 ppm lower for land. The land standard deviation for LMT-
1104 U is 2.3 ppm before subtracting off the 2.1 ppm co-location error. The
1105 difference between the land error for LMT and LMT-U is due to the estimated
1106 size of the co-location error.

1107
1108 Figure 11 shows the seasonal cycle of LMT-U for 3 sites. The differences
1109 between GOSAT and aircraft values at the CAR site in Colorado and LEF in
1110 Wisconsin during the drawdown can be explained by co-location error. The
1111 dotted lines shows CarbonTracker matched to GOSAT (red dotted) or aircraft
1112 (pink dotted) locations/times. The difference between the red dotted and
1113 pink dotted lines estimate the co-location error. If GOSAT were corrected by
1114 this difference, the agreement with aircraft would be much better. The co-
1115 location bias and standard deviation are estimated in Tables 7a and 7b, and
1116 are large compared to the observed GOSAT errors. The error estimates for
1117 GOSAT are corrected by the co-location error. Note that the CAR aircraft
1118 measurements also did not sample down to the boundary layer during this
1119 time period.

1120
1121 The predicted error for LMT-U over land in Table 8b is 2.7 ppm, whereas the
1122 actual error is 2.3 ppm. If LMT and U had zero correlation, the predicted
1123 error (using Eq. 14) would be 3.6 ppm. This is another corroboration of the
1124 positive correlation between the LMT and U errors.

1125
1126 Figure 12 shows LMT – U for February and July in the U.S. averaged over
1127 2010-2014 for February and 2009-2013 for July. LMT – U diagnoses model
1128 vertical transport (Stephens, 2007) and transport of outflow (Deeter, 2013).

1129 Aircraft values for LMT – U are shown as squares. The aircraft patterns are
1130 captured by GOSAT, with discrepancies in July for BNE, CAR, SCA, and SGP
1131 due to co-location error (see CAR plot in Fig. 11). The CarbonTracker model
1132 captures the aircraft patterns very well. The main differences between
1133 GOSAT and CarbonTracker are seen in the southwestern U.S. in July (where
1134 there are no aircraft measurements). Figure 12c-d shows LMT – U for
1135 February and October in the southern hemisphere. The only aircraft site in
1136 this region is Rarotonga, where Fig. 11 shows good agreement for both
1137 CarbonTracker and GOSAT. The patterns in the southern hemisphere show
1138 more differences between CarbonTracker and GOSAT. In February, GOSAT
1139 shows a high gradient in the eastern Pacific and northern South America not
1140 seen in CarbonTracker, and more negative gradient in central and southern
1141 Africa. In October large gradients are seen by GOSAT in South America and
1142 Africa with outflow into the Atlantic, with little seen in CarbonTracker.

1143
1144 LMT-U is predominantly positive in this southern hemisphere region in
1145 October. Vertical transport from the northern hemisphere would
1146 predominantly show up in the U partial column, whereas flux from land or
1147 ocean would predominantly show up in the LMT partial column. An overall
1148 positive value for LMT – U could either suggest that the overall flux is
1149 positive in this month, or that transport from the northern hemisphere was
1150 negative, though the blank space in the Amazon due to cloudy conditions,
1151 where LMT-U is expected to be negative from plant uptake, creates
1152 uncertainty both in this crude estimate and in the formal assimilated results
1153 from GOSAT data.

1154
1155 **6.0 Discussion and conclusions**
1156 GOSAT near-infrared observations provide information to retrieve two partial
1157 column mixing ratios, one from the surface to about 2.5 km (LMT_XCO₂),
1158 and the second above about 2.5 km (U_XCO₂). The two partial columns
1159 have distinct seasonal cycles, with peaks and troughs earlier for the LMT
1160 partial column, and later for the U partial column, as compared to XCO₂
1161 similar to those observed from the NOAA aircraft (e.g. Sweeney et al.,
1162 2015). After bias correction, shown in detail in Appendix A, and following
1163 the same process as the bias correction for ACOS-GOSAT XCO₂, both partial
1164 column mixing ratios show agreement with aircraft, LMT shows agreement
1165 with remote surface observations, and both show improvement over the
1166 GOSAT prior. Single observations for land have observation errors of 3.4,
1167 1.3, and 1.7 ppm for LMT, U, and XCO₂, respectively, and single
1168 observations for ocean have observation errors of 1.5, 0.8, and 0.9 ppm for
1169 LMT, U, and XCO₂, respectively. These errors are significantly reduced with
1170 averaging, though some systematic errors, generally below 1 ppm, remain.
1171 The co-location errors from mismatch of GOSAT versus validation data, as
1172 quantified by CarbonTracker, makes the errors on LMT challenging to

1173 validate, and extension of validation data to the top of the atmosphere with
1174 modeled CO₂ adds uncertainty on the order of 0.4 ppm on the LMT bias.
1175 The value of observing two partial columns can be seen in Fig. 8, where the
1176 GOSAT LMT agrees with remote surface sites whereas neither the prior nor
1177 XCO₂ agree with the surface site, and Figs. 9-10, where surface versus
1178 tropospheric CO₂ are distinguished for source and outflow of African biomass
1179 burning emissions in August and October. The observed LMT CO₂
1180 enhancements with MOPITT multispectral CO and emission ratios are
1181 compared to Akagi et al. (2011), with our emission ratio 2-3% lower in May
1182 and 1-6% higher in August. The LMT-U difference, which can be used to
1183 evaluate model transport error (e.g. Stephens et al., 2007), has also been
1184 evaluated with monthly average error of 0.8 (1.4) ppm for ocean (land).
1185 The new LMT partial column mixing ratio allows the local boundary air to be
1186 distinguished from the free troposphere, captured in the U partial column
1187 mixing ratio, better disentangling local versus remotely influenced signals.
1188

1189
1190 **Acknowledgements:**

1191 This research was funded by NASA and performed under BAER Institute's
1192 ARC-CREST cooperative agreement.
1193

1194 The AJAX team recognizes the support and partnership of H211 L. L. C. and
1195 the NASA Postdoctoral Program; funding for instrumentation and aircraft
1196 integration is gratefully acknowledged from Ames Research Center Director's
1197 funds.
1198

1199 CarbonTracker CT2015 results provided by NOAA ESRL, Boulder, Colorado,
1200 USA from the website at <http://carbontracker.noaa.gov>.
1201

1202 Part of this work was carried out at the Jet Propulsion Laboratory, California
1203 Institute of Technology, under a contract with NASA.
1204

1205 Flights over the Southern Great plains were supported by the Office of
1206 Biological and Environmental Research of the US Department of Energy
1207 under contract no. DE-AC02-05CH11231 as part of the Atmospheric
1208 Radiation Measurement (ARM) Program, ARM Aerial Facility (AAF), and
1209 Terrestrial Ecosystem Science (TES) Program.
1210

1211 TCCON at Lamont and Park Falls are funded by NASA grants NNX14AI60G,
1212 NNX11AG01G, NAG5-12247, NNG05-GD07G, and NASA Orbiting Carbon
1213 Observatory Program, with the DOE ARM program providing technical
1214 support in Lamont and Jeff Ayers providing technical support in Park Falls.
1215

1216
1217

1218 **References**

- 1219
- 1220 Akagi, S. K., Yokelson, R. J., Wiedinmyer, C., Alvarado, M. J., Reid, J. S.,
1221 Karl, T., Crouse, J. D., and Wennberg, P. O.: Emission factors for open and
1222 domestic biomass burning for use in atmospheric models, *Atmos. Chem.*
1223 *Phys.*, 11, 4039-4072, doi:10.5194/acp-11-4039-2011, 2011.
- 1224 Baker, D. F., Law, R. M., Gurney, K. R., Rayner, P., Peylin, P., Denning, A.
1225 S., Bousquet, P., Bruhwiler, L., Chen, Y. H., Ciais, P., Fung, I. Y.,
1226 Heimann, M., John, J., Maki, T., Maksyutov, S., Masarie, K., Prather,
1227 M., Pak, B., Taguchi, S., and Zhu, Z.: TransCom 3 inversion
1228 intercomparison: Impact of trans-port model errors on the interannual
1229 variability of regional CO₂ fluxes, 1988-2003, *Global Biogeochem. Cy.*, 20,
1230 GB1002, doi:10.1029/2004GB002439, 2006.
- 1231 Biraud, S. C., Torn, M. S., Smith, J. R., Sweeney, C., Riley, W. J., and Tans,
1232 P. P.: A multi-year record of airborne CO₂ observations in the US Southern
1233 Great Plains, *Atmos. Meas. Tech.*, 6, 751-763, doi:10.5194/amt-6-751-
1234 2013, 2013.
- 1235 Bowman, K. W., Rodgers, C. D., Kulawik, S. S., Worden, J., Sarkissian, E.,
1236 Osterman, G., Steck, T., Lou, M., Eldering, A., Shephard, M., Worden, H.,
1237 Lampel, M., Clough, S., Brown, P., Rinsland, C., Gunson, M., and Beer, R.:
1238 Tropospheric emission spectrometer: Retrieval method and error analysis,
1239 *IEEE T. Geosci. Remote*, 44(5), 1297-1307, 2006.
- 1240 Chevallier, F., Ciais, P., Conway, T. J., Aalto, T., Anderson, B. E., Bousquet,
1241 P., Brunke, E. G., Ciattaglia, L., Esaki, Y., Frohlich, M., Gomez, A. J., Gomez-
1242 Pelaez, A. J., Haszpra, L., Krummel, P., Langenfelds, R., Leuenberger, M.,
1243 Machida, T., Maignan, F., Matsueda, H., Morgui, J. A., Mukai, H., Nakazawa,
1244 T., Peylin, P., Ramonet, M., Rivier, L., Sawa, Y., Schmidt, M., Steele, P.,
1245 Vay, S. A., Vermeulen, A. T., Wofsy, S., and Worthy, D.: CO₂ surface fluxes
1246 at grid point scale estimated from a global 21-year reanalysis of atmospheric
1247 measurements, *J. Geophys. Res.*, 115, D21307,
1248 doi:10.1029/2010JD013887, 2010.
- 1249 Chevallier, F., Palmer, P. I., Feng, L., Boesch, H., O'Dell, C. W., and
1250 Bousquet, P.: Toward robust and consistent regional CO₂ flux estimates
1251 from in situ and spaceborne measurements of atmospheric CO₂, *Geophys.*
1252 *Res. Lett.*, 41, 1065-1070, doi:10.1002/2013GL058772, 2014.
- 1253 Connor, B. J., Sherlock, V., Toon, G., Wunch, D., and Wennberg, P. O.:
1254 GFIT2: an experimental algorithm for vertical profile retrieval from near-IR
1255 spectra, *Atmos. Meas. Tech.*, 9, 3513-3525, doi:10.5194/amt-9-3513-2016,
1256 2016.

1257 Connor, B. J., H. Boesch, G. Toon, B. Sen, C. Miller, and D. Crisp, Orbiting
1258 Carbon Observatory: Inverse method and prospective error analysis, *J.*
1259 *Geophys. Res.*, 113, D05305, doi:10.1029/2006JD008336, 2008.

1260 Conway, T. J., Tans, P. P., Waterman, L. S., Thoning, K. W., Kitzis, D. R.,
1261 Masarie, K. A., and Zhang, N.: Evidence for interannual variability of the
1262 carbon cycle from the NOAA/CMDL global air sampling network, *J. Geophys.*
1263 *Res.*, 99, 22831-22855, 1994.

1264 Cooperative Global Atmospheric Data Integration Project, 2013, updated
1265 annually. Multi-laboratory compilation of atmospheric carbon dioxide data for
1266 the period 2000-2012 (obspack_co2_1_PROTOTYPE_v1.0.4b_2014-02-13).
1267 Compiled by NOAA Global Monitoring Division: Boulder, Colorado, U.S.A.
1268 Data product accessed at <http://dx.doi.org/10.3334/OBSPACK/1001>.

1269 Crisp, D., B. M. Fisher, C. W. O'Dell, C. Frankenberg, R. Basilio, H. Bösch, L.
1270 R. Brown, R. Castano, B. J. Connor, N. M. Deutscher, A. Eldering, D. Griffith,
1271 M. Gunson, A. Kuze, L. Mandrake, J. McDuffie, J. Messerschmidt, C. E. Miller,
1272 I. Morino, V. Natraj, J. Notholt, D. M. O'Brien, F. Oyafuso, I. Polonsky, J.
1273 Robinson, R. Salawitch, V. Sherlock, M. Smyth, H. Suto, T. E. Taylor, D. R.
1274 Thompson, P. O. Wennberg, D. Wunch, and Y. L. Yung, The ACOS CO₂
1275 retrieval algorithm - Part II: Global XCO₂ data characterization, *Atmospheric*
1276 *Measurement Techniques*, 5(4), 687-707, doi:10.5194/amt-5-687-2012,
1277 2012.

1278 Davies, D., Kumar, S., and Desclotres, J., Global fire monitoring using
1279 MODIS near-real-time satellite data. *GIM International*, 18(4):41-43, 2004.

1280 Deeter, M. N., et al., Operational carbon monoxide retrieval algorithm and
1281 selected results for the MOPITT instrument, *J. Geophys. Res.*, 108(D14),
1282 4399, doi:10.1029/2002JD003186, 2003.

1283 Deeter, M. N., Martinez-Alonso, S., Edwards, D. P., Emmons, L. K., Gille, J.
1284 C., Worden, H. M., Sweeney, C., Pittman, J. V., Daube, B. C., and Wofsy, S.
1285 C.: The MOPITT Version 6 product: algorithm enhancements and validation,
1286 *Atmos. Meas. Tech.*, 7(11), 3623-3632, 2014.

1287 Deng, F., Jones, D. B. A., Walker, T. W., Keller, M., Bowman, K. W., Henze,
1288 D. K., Nassar, R., Kort, E. A., Wofsy, S. C., Walker, K. A., Bourassa, A. E.,
1289 and Degenstein, D. A.: Sensitivity analysis of the potential impact of
1290 discrepancies in stratosphere-troposphere exchange on inferred sources and
1291 sinks of CO₂, *Atmos. Chem. Phys.*, 15, 11773-11788, doi:10.5194/acp-15-
1292 11773-2015, 2015.

1293 Denning, A. S., Collatz, G. J., Zhang, C., Randall, D. A., Berry, J. A.,
1294 Sellers, P. J., Colello, G. D., and Dazlich, D. A.: Simulations of terrestrial
1295 carbon metabolism and atmospheric CO₂ in a general circulation model. Part
1296 2: simulated CO₂ concentrations, *Tellus*, 48B, 543-567, 1996.

1297 Dohe, S., Measurements of atmospheric CO₂ columns using ground-based
1298 FTIR spectra, Doctor of Science dissertation, Karlsruhe Institute for
1299 Technology, Karlsruhe, Germany, 2013.

1300 Feng, L., Palmer, P. I., Parker, R. J., Deutscher, N. M., Feist, D. G., Kivi, R.,
1301 Morino, I., and Sussmann, R.: Estimates of European uptake of CO₂ inferred
1302 from GOSAT X-CO₂ retrievals: sensitivity to measurement bias inside and
1303 outside Europe, *Atmospheric Chemistry And Physics*, 16, 1289-1302,
1304 doi:10.5194/acp-16-1289-2016, 2016.

1305 Giglio, L., J. Descloitres, C. O. Justice, and Y. J. Kaufman, An enhanced
1306 contextual fire detection algorithm for MODIS. *Remote Sensing of*
1307 *Environment*, 87:273-282, 2003.

1308 GLOBALVIEW-CO₂, Cooperative Global Atmospheric Data Integration
1309 Project, updated annually. Multi-laboratory compilation of atmospheric
1310 carbon dioxide data for the period 2000-2012
1311 (obspack_co2_1_PROTOTYPE_v1.0.4b_2014-02-13). Compiled by NOAA
1312 Global Monitoring Division: Boulder, Colorado, U.S.A. Data product accessed
1313 at <http://dx.doi.org/10.3334/OBSPACK/1001>, 2013.
1314

1315 Guerlet, S., Butz, A., Schepers, D., Basu, S., Hasekamp, O. P., Kuze, A.,
1316 Yokota, T., Blavier, J.-F., Deutscher, N. M., Griffith, D. W. T., Hase, F., Kyro,
1317 E., Morino, I., Sherlock, V., Sussmann, R., Galli, A., Aben, I., *J. Geophys.*
1318 *Res. Atmos.*,118,4887-4905,doi:10.1002/jgrd.50332, 2013.

1319 Gurney, K. R., Law, R. M., Denning, A. S., Rayner, P. J., Baker, D.,
1320 Bousquet, P., Bruhwiler, L., Chen, Y.-H., Ciais, P., Fan, S., Fung, I. Y., Gloor,
1321 M., Heimann, M., Higuchi, K., John, J., Maki, T., Maksyutov, S., Masarie, K.,
1322 Peylin, P., Prather, M., Pak, B. C., Randerson, J., Sarmiento, J., Taguchi, S.,
1323 Takahashi, T., and Yuen, C.-W.: Towards robust regional estimates of CO₂
1324 sources and sinks using atmospheric transport models, *Nature*, 415, 626-
1325 630, 2002.

1326 Hamill, P., L. Iraci, E. Yates, W. Gore, T. P. Bui, T. Tanaka, and M.
1327 Loewenstein (2016), A new instrumented airborne platform for atmospheric
1328 research, *Bulletin of the American Meteorological Society*. vol. 97, no. 3,
1329 doi:10.1175/BAMS-D-14-00241.1.

1330 Houweling, S., Baker, D., Basu, S., Boesch, H., Butz, A., Chevallier, F.,
1331 Deng, F., Dlugokencky, E. J., Feng, L., Ganshin, A., Hasekamp, O., Jones,
1332 D., Maksyutov, S., Marsha, J., Oda, T., O'Dell, C. W., Oshchepkov, S.,
1333 Palmer, P. I., Peylin, P., Poussi, Z., Reum, F., Takagi, H., Yoshida, Y., and
1334 Zhuravlev, R.: An intercomparison of inverse models for estimating sources
1335 and sinks of CO₂ using GOSAT measurements, *J. Geophys. Res. Atmos.*,
1336 120, 5253-5266, 2015.

1337 Inoue, M., Morino, I., Uchino, O., Miyamoto, Y., Yoshida, Y., Yokota,
1338 T., Machida, T., Sawa, Y., Matsueda, H., Sweeney, C., Tans, P. P., Andrews,
1339 A. E., Biraud, S. C., Tanaka, T., Kawakami, S., and Patra, P. K.:
1340 Validation of XCO₂ derived from SWIR spectra of GOSAT TANSO-FTS with
1341 aircraft measurement data, *Atmos. Chem. Phys.*, 13, 9771-9788, doi:
1342 10.5194/acp-13-9771-2013, 2013.

1343 Karion, A., C. Sweeney, P. Tans, and T. Newberger: AirCore: An innovative
1344 atmospheric sampling system. *J. Atmos. Oceanic Technol.*, 27, 1839-1853,
1345 DOI: <http://dx.doi.org/10.1175/2010JTECHA1448.1>, 2010.

1346 Kulawik, S. S., Osterman, G., Jones, D. B. A., and Bowman, K.W.,
1347 Calculation of altitude-dependent Tikhonov constraints for TES nadir
1348 retrievals, *IEEE T. Geosci. Remote*, 44(5), 1334-1342, 2006.

1349 Kulawik, S., Wunch, D., O'Dell, C., Frankenberg, C., Reuter, M., Oda, T.,
1350 Chevallier, F., Sherlock, V., Buchwitz, M., Osterman, G., Miller, C. E.,
1351 Wennberg, P. O., Griffith, D., Morino, I., Dubey, M. K., Deutscher, N. M.,
1352 Notholt, J., Hase, F., Warneke, T., Sussmann, R., Robinson, J., Strong, K.,
1353 Schneider, M., De Mazière, M., Shiomi, K., Feist, D. G., Iraci, L. T., and Wolf,
1354 J.: Consistent evaluation of ACOS-GOSAT, BESD-SCIAMACHY,
1355 CarbonTracker, and MACC through comparisons to TCCON, *Atmos. Meas.*
1356 *Tech.*, 9, 683-709, doi:10.5194/amt-9-683-2016, 2016.

1357 Kuze, A., Suto, H., Shiomi, K., Kawakami, S., Tanaka, M., Ueda, Y.,
1358 Deguchi, A., Yoshida, J., Yamamoto, Y., Kataoka, F., Taylor, T. E., and Buijs,
1359 H. L.: Update on GOSAT TANSO-FTS performance, operations, and data
1360 products after more than 6 years in space, *Atmos. Meas. Tech.*, 9, 2445-
1361 2461, doi:10.5194/amt-9-2445-2016, 2016.

1362 Lauvaux, T. and Davis, K. J.: Planetary boundary layer errors in mesoscale
1363 inversions of column-integrated CO₂ measurements, *J. Geophys. Res.-*
1364 *Atmos.*, 119, 490-508, doi:10.1002/2013jd020175, 2014.

1365 Liu, J., I. Fung, E. Kalnay, and J. S. Kang, CO transport uncertainties from
1366 the uncertainties in meteorological fields, *Geophys. Res. Lett.*, 38, L12808,
1367 doi:10.1029/2011GL047213, 2011.

1368 Liu, J., Bowman, K. W., and Henze, D. K.: Source-receptor relationships of
1369 column-average CO₂ and implications for the impact of observations on flux
1370 inversions, *J. Geophys. Res. Atmos.*, 120, 5214-5236, 2015.

1371 Membrive, O., Crevoisier, C., Sweeney, C., Danis, F., Hertzog, A., Engel, A.,
1372 Bönisch, H., and Picon, L.: AirCore-HR: A high resolution column sampling to
1373 enhance the vertical description of CH₄ and CO₂, *Atmos. Meas. Tech.*
1374 *Discuss.*, doi:10.5194/amt-2016-236, in review, 2016.

1375 Kuai L., Wunch, D., Shia, R.-L., Connor, B., Miller, C., and Yung, Y.:
1376 Vertically constrained CO₂ retrievals from TCCON measurements, *J. Quant.*
1377 *Spectrosc. Ra.*, 113, 1753-1761, 2012.

1378 Miller, C. E., D. Crisp, P. L. DeCola, S. C. Olsen, J. T. Randerson, A. M.
1379 Michalak, A. Alkhaled, P. Rayner, D. J. Jacob, P. Suntharalingam, D. B. A.
1380 Jones, A. S. Denning, M. E. Nicholls, S. C. Doney, S. Pawson, H. Boesch, B. J.
1381 Connor, I. Y. Fung, D. O'Brien, R. J. Salawitch, S. P. Sander, B. Sen, P.
1382 Tans, G. C. Toon, P. O. Wennberg, S. C. Wofsy, Y. L. Yung, and R. M. Law,
1383 Precision requirements for space-based XCO₂ data, *J. Geophys. Res.*, 112,
1384 D10314, doi:10.1029/2006JD007659, 2007.

1385 Nehrkorn, T., J. Eluszkiewicz, S. C. Wofsy, J. C. Lin, C. Gerbig, M. Longo and
1386 S. Freitas, Coupled Weather Research and Forecasting-Stochastic-Time-
1387 Inverted Lagrangian Transport Model, *Meteorol. Atmos. Phys.*, 107: 51-64,
1388 2010.

1389 O'Brien, D. M., and P. J. Rayner, Global observations of the carbon budget,
1390 2, CO₂ concentrations from differential absorption of reflected sunlight in the
1391 1.61 μm band of CO₂, *J. Geophys. Res.*, 107(D18), 4354,
1392 doi:10.1029/2001JD000617, 2002.

1393 Peters, Wouter, Jacobson, Andrew R., Sweeney, Colm, Andrews, Arlyn E.,
1394 Conway, Thomas J., Masarie, Kenneth, Miller, John B., Bruhwiler, Lori M. P.,
1395 Petron, Gabrielle, Hirsch, Adam I., Worthy, Douglas E. J., van der Werf,
1396 Guido R., Randerson, James T., Wennberg, Paul O., Krol, Maarten C., and
1397 Tans, Pieter P.: An atmospheric perspective on North American carbon
1398 dioxide exchange: CarbonTracker, *Proceedings Of The National Academy Of*
1399 *Sciences Of The United States Of*, 104, 18925-18930,
1400 doi:10.1073/pnas.0708986104, 2007.

1401 Prather, M. J.; Zhua, X; Strahan, SE; Steenrod, SD; Rodriguez, JM,
1402 Quantifying errors in trace species transport modeling. *Proceedings of the*
1403 *National Academy of Sciences of the United States of America* 105(50),
1404 19617-19621. DOI: 10.1073/pnas.0806541106, Dec 16, 2008

1405 Rayner, P. J., and O'Brien, D. M., The utility of remotely sensed CO₂
1406 concentration data in surface source inversions (vol 28, pg 175, 2001),
1407 *Geophys. Res. Lett.*, 28, 2429-2429, doi:10.1029/2001GL013115, 2001.

1408 Rodgers, C. D. In: *Inverse methods for atmospheric sounding: theory and*
1409 *practice*. London. WorldScientific, 2000.

1410 Steck, T. and von Clarmann, T., Constrained profile retrieval applied to the
1411 observation mode of the Michelson Interferometer for Passive Atmospheric
1412 Sounding, *Appl. Opt.*, 40, 3559-3571, 2001.

1413 Stephens, B. B., Gurney, K. R., Tans, P. P., Sweeney, C., Peters, W.,
1414 Bruhwiler, L., Ciais, P., Ramonet, M., Bousquet, P., Nakazawa, T., Aoki, S.,

1415 Machida, T., Inoue, G., Vinnichenko, N., Lloyd, J., Jordan, A., Heimann, M.,
1416 Shibistova, O., Langenfelds, R. L., Steele, L. P., Francey, R. J., and Denning,
1417 A. S.: Weak northern and strong tropical land carbon uptake from vertical
1418 profiles of atmospheric CO₂, *Science*, 2007 Jun 22;316(5832), 1732 - 5,
1419 2007.

1420 Sweeney, C., A. Karion, S. Wolter, T. Newberger, D. Guenther, J. A. Higgs,
1421 A. E. Andrews, P. M. Lang, D. Neff, E. Dlugokencky, J. B. Miller, S. A.
1422 Montzka, B. R. Miller, K. A. Masarie, S. C. Biraud, P. C. Novelli, M. Crotwell,
1423 A. M. Crotwell, K. Thoning, and P. P. Tans (2015), Seasonal climatology of
1424 CO₂ across North America from aircraft measurements in the NOAA/ESRL
1425 Global Greenhouse Gas Reference Network, *Journal of Geophysical*
1426 *Research-Atmospheres*, 120(10), 5155-5190.doi: 10.1002/2014jd022591

1427 Tanaka, T., E. Yates, L. Iraci, M. Johnson, W. Gore, J. Tadic, M. Loewenstein,
1428 A. Kuze, C. Frankenberg, A. Butz, and Y. Yoshida (2015), Two years
1429 comparison of airborne measurements of CO₂ and CH₄ with GOSAT at
1430 Railroad Valley, Nevada, in press at *IEEE Transactions on Geoscience and*
1431 *Remote Sensing*. doi: 10.1109/TGRS.2016.2539973.

1432 Thoning, K. W., Tans, P. P., and Komhyr, W. D.: Atmospheric Carbon
1433 Dioxide at Mauna Loa Observatory 2. Analysis of the NOAA GMCC Data,
1434 1974–1985, *J. Geophys. Res.*, 94, 8549–8565,
1435 doi:10.1029/JD094iD06p08549, 1989.

1436 Tikhonov, A.: On the solution of incorrectly stated problems and a method of
1437 regularization, *Dokl. Acad. Nauk SSSR*, vol. 151, pp. 501 - 504, 1963.

1438 Twomey, S.: On the Numerical Solution of Fredholm Integral Equations of
1439 the First Kind by the Inversion of the Linear System Produced by
1440 Quadrature, *Journal of the Association for Computing Machinery*, 1701. 10
1441 NO. 1, pp. 97 - 101, 1963.

1442 von Clarmann, T., Glatthor, N., Grabowski, U., Hopfner, M., Kellmann, S.,
1443 Kiefer, M., Linden, A., Mengistu Tsidu, G., Milz, M., Steck, T., Stiller,
1444 G. P., Wang, D. Y., Fischer, H., Funke, B., Gil-Lopez, S., and Lopez-
1445 Puertas, M.: Retrieval of temperature and tangent altitude pointing from
1446 limb emission spectra recorded from space by the Michelson Interferometer
1447 for Passive Atmospheric Sounding (MIPAS), *J. Geophys. Res.*, 108, 4736,
1448 doi:10.1029/2003JD003602, 2003.

1449 Wennberg, P. O., C. Roehl, D. Wunch, G. C. Toon, J.-F. Blavier, R.
1450 Washenfelder, G. Keppel-Aleks, N. Allen, J. Ayers. 2014. TCCON data from
1451 Park Falls, Wisconsin, USA, Release GGG2014R0. TCCON data archive,
1452 hosted by the Carbon Dioxide Information Analysis Center, Oak Ridge
1453 National Laboratory, Oak Ridge, Tennessee, U.S.A.
1454 <http://dx.doi.org/10.14291/tcccon.ggg2014.parkfalls01.R0/1149161>

1455 Wennberg, P. O. Wunch, D. Roehl, C., Blavier, J.-F., Toon, G. C., Allen, N.,
1456 Dowell, P., Teske, K., Martin, C., and Martin., J., TCCON data from Lamont,
1457 Oklahoma, USA, Release GGG2014R0. TCCON data archive, hosted by the
1458 Carbon Dioxide Information Analysis Center, Oak Ridge National Laboratory,
1459 Oak Ridge, Tennessee, U.S.A.
1460 <http://dx.doi.org/10.14291/tccon.ggg2014.lamont01.R0/1149159>

1461 Wofsy, S. C., Daube, B. C., Jimenez, R., Kort, E., Pittman, J. V., Park, S.,
1462 Commane, R., Xiang, B., Santoni, G., Jacob, D., Fisher, J., Pickett-Heaps, C.,
1463 Wang, H., Wecht, K., Wang, Q.-Q., Stephens, B. B., Shertz, S., Watt, A. S.,
1464 Romashkin, P., Campos, T., Haggerty, J., Cooper, W. A., Rogers, D., Beaton,
1465 S., Hendershot, R., Elkins, J. W., Fahey, D. W., Gao, R. S., Moore, F.,
1466 Montzka, S. A., Schwarz, J. P., Perring, A. E., Hurst, D., Miller, B. R.,
1467 Sweeney, C., Oltmans, S., Nance, D., Hints, E., Dutton, G., Watts, L. A.,
1468 Spackman, J. R., Rosenlof, K. H., Ray, E. A., Hall, B., Zondlo, M. A., Diao,
1469 M., Keeling, R., Bent, J., Atlas, E. L., Lueb, R., and Mahoney, M. J.: HIPPO
1470 Merged 10-second Meteorology, Atmospheric Chemistry, Aerosol Data
1471 (R_20121129). Carbon Dioxide Information Analysis Center, Oak Ridge
1472 National Laboratory, Oak Ridge, Tennessee, USA,
1473 [doi:10.3334/CDIAC/hippo_010](https://doi.org/10.3334/CDIAC/hippo_010), 2012.

1474 Worden, H. M., Deeter, M. N., Edwards, D. P., Gille, J. C., Drummond, J. R.,
1475 and N?d?lec, P.: Observations of near-surface carbon monoxide from space
1476 using MOPITT multispectral retrievals, *Journal Of Geophysical Research*
1477 (*Atmospheres*), 115(d14), 1831-18314, 2010.

1478 Worden, J., Kulawik, S. S., Shephard, M. W., Clough, S. A., Worden, H.,
1479 Bowman, K. and Goldman, A.. Predicted errors of tropospheric emission
1480 spectrometer nadir retrievals from spectral window selection, *Journal of*
1481 *Geophysical Research-Atmospheres*, 109, (D9), 2004.

1482 Wunch, D., Toon, G.C., Blavier, J.-F.L., Washenfelder, R.A., Notholt, J.,
1483 Connor, B.J., Griffith, D.W.T., Sherlock, V., Wennberg, P.O.: The Total
1484 Carbon Column Observing Network. *Phil. Trans. R. Soc. A*, 369,
1485 [doi:10.1098/rsta.2010.0240](https://doi.org/10.1098/rsta.2010.0240), 2011a.

1486 Wunch, D., Wennberg, P. O., Toon, G. C., Connor, B. J., Fisher, B.,
1487 Osterman, G. B., Frankenberg, C., Mandrake, L., O'Dell, C., Ahonen, P., and
1488 et al.: A method for evaluating bias in global measurements of CO₂ total
1489 columns from space, *Atmospheric Chemistry and Physics*, 11, 12 317-12
1490 337, [doi:10.5194/acp-11-12317-2011](https://doi.org/10.5194/acp-11-12317-2011), URL [http://dx.doi.org/10.5194/acp-](http://dx.doi.org/10.5194/acp-11-12317-2011)
1491 [11-12317-2011](http://dx.doi.org/10.5194/acp-11-12317-2011), 2011b.

1492 Yokota, T., Yoshida, Y., Eguchi, N., Ota, Y., Tanaka, T., Watanabe, H., and
1493 Maksyutov, S.: Global Concentrations of CO₂ and CH₄ Retrieved from
1494 GOSAT: First Preliminary Results, *Sola*, 5, 160-163, 2009.

1495 **Appendix A. Bias Correction**

1496
1497 The ACOS-GOSAT XCO₂ product undergoes bias correction (Wunch et al.,
1498 2011) which significantly improves the errors (Kulawik, 2016). We apply
1499 this same technique to correct the LMT product. Land nadir mode ("land")
1500 and ocean glint mode ("ocean") are bias corrected separately for LMT.
1501 Following the LMT correction, U is corrected by subtracting the LMT partial
1502 column from ACOS-GOSAT corrected XCO₂, thus maintaining consistency
1503 between the [LMT,U] partial columns and the total XCO₂ column after bias-
1504 correction. This is done because the XCO₂ bias correction has been checked
1505 against TCCON which has sensitivity throughout the entire column, and
1506 because there is uncertainty in the "true" U used for validation, which is
1507 calculated from aircraft extended with the CarbonTracker model above about
1508 5 km, composing a large part of the U partial column.

1509
1510 To determine the LMT bias correction, GOSAT and aircraft data are matched
1511 using dynamic coincidence criteria (Wunch, 2011), and the difference
1512 between GOSAT LMT and aircraft LMT is calculated for all pairs in either land
1513 or ocean groups versus each potential parameter. In order to identify the
1514 critical bias-predicting parameters, for those cases for which this difference
1515 has a clear slope, a bias correction is applied iteratively, where the strongest
1516 parameter dependence is corrected before the next parameters are tested.
1517 At the end all parameters are fit simultaneously. Filters are applied to flag
1518 the data as bad when the bias is significant even after correction. The
1519 parameters considered for bias correction are: delta_grad_co2, albedo_1,
1520 albedo_2, albedo_3, albedo_slope_1, albedo_slope_2, albedo_slope_3,
1521 aod_dust, aod_ice, aod_total, b1offset, ice_height, surfacePressure_xa,
1522 surfacePressureDiff, co2_ratio, dp_cld, h2o_ratio, s32, xco2_error, LMT_dofs
1523 (degrees of freedom for LMT), u_dofs (degrees of freedom for U), xco2_dofs,
1524 asza, lza, and delta_grad_co2_prime. These parameters are described in
1525 the ACOS-GOSAT v3.5 user's guide with the exception of
1526 delta_grad_co2_prime which is defined as delta_grad_co2 with the value set
1527 to 50 when it is greater than 50 for land, and the value set to -10 when it is
1528 greater than -10 for ocean. Two figures of merit were considered for the
1529 cutoffs and bias fits, (1) bias variability by location and season and (2) the
1530 single-observation standard deviation. The former is the standard deviation
1531 of the biases calculated in 4 seasons and for each location/campaign. For
1532 both of these figures of merit, smaller is better.

1533
1534 By far the strongest bias is related to delta_grad_CO2. This parameter is
1535 the difference between the retrieved CO₂ and a priori dry-air molefraction
1536 between the surface and vertical level 13 (approximately 630 hPa for
1537 soundings near sea level), and represents the slope of the retrieved CO₂
1538 profile in the troposphere. The resulting coefficient for this term is 0.396 for

1539 ocean and 0.310 for land soundings. This indicates that, for ocean,
1540 approximately 40% of the CO₂ attributed to the surface should be moved
1541 from LMT to U, indicating that possibly (a) the troposphere is constrained
1542 too much relative to the surface, (b) an issue with the forward model, such
1543 as systematic errors in spectroscopy, or (c) some other retrieval artefact.
1544 The bias correction coefficient for delta_grad_CO₂ for simulated OCO-2 land
1545 data is 0.29, very similar to the value of 0.31 for actual GOSAT data
1546 (Kulawik, unpublished result). The simulated runs have no spectroscopic
1547 error or other forward model errors, so the need for delta_grad_CO₂
1548 correction is likely not driven by forward model errors, but could be a
1549 consequence of way the CO₂ profile is constrained in the retrieval through
1550 the constraint matrix, which allows a lot of variability near the surface and
1551 damps variability in the mid-troposphere. This could prejudice the retrieval
1552 system to attribute radiance variations to CO₂ variations at the surface
1553 rather than elsewhere in the profile, with the delta_grad_CO₂ correction
1554 factor undoing this tendency. This relationship should be explored further
1555 using a simulated system with different constraint matrices.

1556
1557 The filtering cutoffs and bias terms are shown in Table A1. The errors
1558 calculated by the bootstrap method (Rubin, 1981). The effects of the cutoffs
1559 and bias corrections from Table A1 on biases and standard deviations is
1560 shown in Table A2.

1561
1562 The overall land bias is not zero because the land bias constant correction
1563 undergoes a final step to harmonize land and ocean observations by
1564 matching GOSAT values for pairs of close land and ocean observations. The
1565 results (using the final bias correction) for different matching criteria are: 1
1566 degree and 1 hour (25 matches, bias -0.54 ppm in LMT and -0.96 ppm in
1567 XCO₂), 2 degrees and 24 hours (295 matches, 0.17 ppm in LMT and -0.61
1568 ppm in XCO₂), 4 degrees and 48 hours (4095 matches, 1.17 ppm in LMT and
1569 -0.09 ppm in XCO₂), and using dynamic coincidence criteria (422,542
1570 matches, 0.29 ppm in LMT, -0.42 in XCO₂). Using the assumption that there
1571 is no bias in XCO₂, the 4 degree, 48 hours result is used, and 1.17 ppm is
1572 added to the LMT constant bias for land. This constant bias is subtracted
1573 from LMT, then the LMT partial column is subtracted from XCO₂ to generate
1574 the corrected U partial column. The 1.2 ppm change in the land bias to
1575 match ocean results gives an idea of the size of the uncertainty in the bias.

1576
1577 As seen from Tables A3a and A3b, all bias corrections are superior to the
1578 uncorrected dataset, and all correction tests perform similarly in the bias
1579 standard deviation and mean standard deviation, but with variability in the
1580 overall bias, depending on the development set that is used. The overall
1581 bias has some uncertainty on the order of 0.5 ppm.

1582

1583 Another potential error source that is quantified is the effect of different
1584 profile extension schemes above aircraft observations. The ESRL aircraft
1585 measurements go up to 5-8 km above ground, and the HIPPO observations
1586 go up to 9-13 km above ground. 4 different profile extension methods are
1587 tried above the aircraft: using (1) the GOSAT a priori profile, (2) extending
1588 the top aircraft measurement to the tropopause pressure with the GOSAT
1589 prior above this, (3) the CT2015 model, and (4) extending the top aircraft
1590 measurement to the tropopause pressure with the CT2015 model above this.
1591 Table A4 shows the land and ocean characteristics with each of the profile
1592 extension type. The main effect is on the overall bias (up to 0.4 ppm) in the
1593 comparisons. One issue is likely in the top 4 levels, from which a difference
1594 between a priori and the true profile would propagate as a bias.

1595
1596 Table A5 compares the extension with AirCore versus CarbonTracker.
1597 AirCore measures from the surface up to as high as 13 hPa, meaning that all
1598 but the top GOSAT pressure level is measured. 8 AirCore observations are
1599 found to matches aircraft and GOSAT observations within 3 degrees
1600 longitude, 5 degrees latitude, and 7 days. 6 of the matches are at SGP and
1601 2 are at CAR. For these matches, the aircraft observations are extended
1602 either with AirCore (using CarbonTracker at only the top pressure level) or
1603 CarbonTracker. The finding is similar to the finding from Table A4, that
1604 there is uncertainty in the overall bias of 0.4 ppm, but that the standard
1605 deviation is not affected by which extension is used. The reason for 0.4 ppm
1606 bias is that the CarbonTracker stratosphere is high compared to AirCore for
1607 these 8 observations. This propagates into a high bias in the "true" U and a
1608 low bias in the "true" LMT, through the averaging kernel. Because there is
1609 uncertainty in the true value of the stratosphere that is used to extend the
1610 aircraft profiles, there is some uncertainty in the overall bias of GOSAT LMT
1611 and U on the order of 0.4 ppm.

1612
1613 There were several ways that the developed bias correction was insulated
1614 from the validation: (1) the bias correction uses dynamic coincidence
1615 criteria (Wunch, 2011), whereas the comparisons to validation data use
1616 geometric coincidence criteria (± 5 degrees latitude and longitude, and ± 1
1617 week). The overlap between these two sets is about 50%. (2) remote
1618 ocean surface sites were not used to develop the bias correction. These
1619 locations are expected to have good mixing between the surface and 2.5
1620 km, but since we do not have profiles at these locations, these observations
1621 are not used for direct validation. These comparisons between GOSAT and
1622 remote surface sites show excellent improvement over the GOSAT prior. (3)
1623 No data over the southern hemisphere biomass burning is used in the bias
1624 correction, and GOSAT compares very well to MOPITT in this region. (4)
1625 Comparisons were made, taking out observations used in the bias correction

1626 at SGP, where there are plenty of matches. These comparisons were as
1627 good as the full set.

1628

1629 The mean and standard deviation of the bias correction is -11.4 ± 7.6 ,
1630 2.7 ± 2.7 ppm for LMT and U land, respectively and -1.0 ± 3.1 ppm, -1.7 ± 0.9
1631 ppm for LMT and U ocean, respectively. The mean and standard deviations
1632 of the bias correction for XCO₂ are: -0.6 ± 1.0 ppm for land and -0.6 ± 0.6 for
1633 ocean. The bias corrections are larger for the partial columns than for XCO₂;
1634 the size and variability of the bias correction is an indication of its
1635 importance.

1636

1637

1638

1639 **Appendix B. Detailed comparisons by site and campaign**

1640

1641 In addition to the averaged results provided previously, Table B1 below
1642 breaks down the validation results for each individual station. This table
1643 could be useful for diagnosing outliers in the comparisons, looking at
1644 correlations of site-to-site biases or standard deviations in LMT and U.

1645

1646

Table 1. Sites used for validation in this paper

Type	Site	Site name	Country	Latitude	Longitude	match
aircraft	AOA	Aircraft Observation of Atmospheric trace gases, JMA	Japan	28.8N	148.4E	77
aircraft	BNE	Beaver Crossing, Nebraska	USA	40.8N	97.2W	452
aircraft	CAR	Briggsdale, Colorado	USA	40.4N	104.3W	1599
aircraft	CMA	Cape May, New Jersey	USA	38.8N	74.3W	536
aircraft	DND	Dahlen, North Dakota	USA	47.5N	99.2W	415
aircraft	ESP	Estevan Point, British Columbia	Canada	49.4N	126.5W	142
aircraft	ETL	East Trout Lake, Saskatchewan	Canada	54.4N	104.9W	237
aircraft	HIL	Homer, Illinois	USA	40.1N	87.9W	1039
aircraft	LEF	Park Falls, Wisconsin	USA	45.9N	90.3W	717
aircraft	NHA	Worcester, Massachusetts	USA	42.9N	70.5W	430
aircraft	PFA	Poker Flats, Alaska	USA	65.1N	147.3W	107
aircraft	RTA	Rarotonga	Cook Is.	21.3S	159.8W	228
aircraft	SCA	Charleston, South Carolina	USA	32.8N	79.6W	764
aircraft	SGP	Southern Great Plains, Oklahoma	USA	36.6N	97.5W	6066
aircraft	TGC	Sinton, Texas	USA	27.7N	96.9W	941
aircraft	THD	Trinidad Head, California	USA	41.1N	124.2W	226
aircraft	WBI	West Branch, Iowa	USA	41.7N	91.4W	602
Surface	MNM	Minamitorishima	Japan	24.3N	154.0E	66,733
Surface	MLO	Mauna Loa, Hawaii	USA	19.5N	155.6W	940
Surface	KUM	Cape Kumukahi, Hawaii	USA	19.5N	154.8W	876
Surface	GMI	Mariana Islands	Guam	13.4N	144.6E	1043
Surface	CHR	Christmas Island	Kiribati	1.7N	157.2W	1038
Surface	ASC	Ascension Island	U.K.	8.0S	14.4W	2125
Surface	SMO	Tutuila	American Samoa	14.2S	170.6W	4267
Surface	EIC	Easter Island	Chile	27.2S	109.4W	432
Surface	SEY	Mahe Island	Seychelles	4.7S	55.5E	679
Aircraft	HIPPO 2S	November, 2009, Pacific Ocean		0-39S	161-178W	156
Aircraft	HIPPO 2N	November, 2009, Pacific Ocean		6-41S	151-179E	277
Aircraft	HIPPO 3S	April, 2010, Pacific Ocean		16S-14N	160-170W	68
Aircraft	HIPPO 3N	April, 2010, Pacific Ocean		16S-8N	161-170W	71
Aircraft	HIPPO 4S	June, 2011, Pacific Ocean		5-15N	160-164W	13

Aircraft	HIPPO	July, 2011, Pacific Ocean		4-44N	134E-172W	1054
Aircraft	HIPPO	August, 2011		3S-15N	160-166W	20
Aircraft	HIPPO	September, 2011		18S-21N	156-169W	363
Aircraft	AJAX	California/Nevada	USA	37.3-38.5N	116-121W	35

1648

1649

1650 Table 2

1651 Predicted errors and degrees of freedom for LMT and U. As seen in Table 3,
 1652 the predicted errors are much larger than the actual errors.

	land	ocean
LMT error (ppm)	4.3 ppm	4.4 ppm
U error (ppm)	1.7 ppm	1.7 ppm
U,LMT pred. error correlation	-0.72	-0.78
LMT DOFs	0.86	0.86
U DOFs	0.84	0.83

1653

1654

1655 Table 3. Definition of comparison terms

1656 Co-location bias: The mean difference of CarbonTracker matched to the
 1657 satellite minus CarbonTracker matched to the aircraft. A persistent
 1658 co-location bias indicates sampling differences. For example, a
 1659 seasonal co-location error was found to result from time-of-day
 1660 difference between validation data collection time and the GOSAT
 1661 overpass (see Fig. 11). For ocean flasks, where the validation data is
 1662 only at the surface, vertical co-location bias of 0.3 ppm results from
 1663 sampling difference between the model sampled with the LMT
 1664 averaging kernel and the model at the surface (see Table 4).

1665 Co-location error, ε_{coloc} : The standard deviation of CarbonTracker matched
 1666 to the satellite minus CarbonTracker matched to the aircraft or surface
 1667 flask. This represents error introduced by the satellite not observing
 1668 at the exact time and location of the validation data. The surface
 1669 flasks have an additional term, the standard deviation of
 1670 CarbonTracker sampled with the LMT averaging kernel and
 1671 CarbonTracker sampled at the surface.

1672 Correlated error: Correlated error is the component of the standard
 1673 deviation which does not reduce when additional GOSAT observations
 1674 are averaged. Think of this quantity as a regional, daily (or a bit
 1675 longer) bias. See Eq. 11.

1676 Random error: Random error is the component of the standard deviation
 1677 that reduces when more GOSAT observations are averaged. See Eq.
 1678 11.

1679 GOSAT bias: The mean of GOSAT minus the validation data. The bias is
 1680 calculated by latitude, season, and time. Different biases at different
 1681 locations can cause phantom fluxes.

1682 GOSAT error: The standard deviation of GOSAT minus the validation data

1683 Predicted error: The error predicted by the GOSAT optimal estimation
 1684 retrieval system.

1685 Prior bias: The mean of the GOSAT prior minus the validation data

1686 True mean: The mean of all validation data at that site. For stations, the
 1687 mean is averaged over time, and for each HIPPO campaign, it is
 1688 averaged over latitude/longitude.

1689 True variability: The standard deviation of the validation data for each
 1690 station or campaign. The true variability is higher over land than
 1691 ocean, or for the LMT versus U. Observations with larger error will be
 1692 more useful at locations where there is higher true variability.

1693 ($n=1$), ($n=15$): This specifies how many GOSAT observation are averaged
 1694 prior to the calculation of bias or error. All GOSAT observations that
 1695 are averaged match the same validation data point. The size of n
 1696 matters for errors, with larger numbers averaged resulting in smaller
 1697 errors (but not reducing as fast as the square root of n).

1698
 1699
 1700 Table 4. Biases versus validation data. See Table 3 for terminology used in
 1701 this table. Note that all data is averaged by location or campaign. The \pm
 1702 represents the variability of the bias by location or campaign, a key metric in
 1703 the data quality.

	Type	Ocean surface (ppm)	HIPPO Ocean (ppm)	ESRL Ocean (ppm)	ESRL Land (ppm)	AJAX Land (ppm)
co-location bias	LMT	-0.3±0.3 -0.3±0.8	-0.3±0.2	-0.3±0.4	-0.6±0.7	-0.6
	U		0.1±0.1	-0.1±0.1	0.0±0.2	0.0
	XCO ₂		0.0±0.1	-0.1±0.1	-0.1±0.3	-0.1
true mean	LMT	391.3±1.6	392.2±1.6	391.7±1.1	392.2±3.1	393.6
	U		391.1±1.2	391.3±1.6	391.2±0.6	392.2
	XCO ₂		391.4±1.3	391.4±1.5	391.5±1.1	392.4
prior bias	LMT	-0.8±1.5	0.1±2.4	-1.5±4.5	-0.4±1.2	-1.4
	U		1.2±0.1	-1.2±1.6	0.6±0.6	0.4
	XCO ₂		0.9±1.4	0.4±2.3	-0.2±0.6	-0.1
GOSAT bias	LMT	1.1±1.1	0.1±0.3	0.3±0.7	-0.2±1.0	0.4
	U		0.1±0.3	0.7±0.1	0.3±0.9	1.0
	XCO ₂		0.1±0.2	0.6±0.4	0.1±0.9	0.7

1704
1705
1706
1707

Table 5. Standard deviations versus validation data. See Table 3 for definitions of terms. The co-location errors have been subtracted out from the GOSAT errors.

	Type	Ocean surface (ppm)	HIPPO Ocean (ppm)	ESRL Ocean (ppm)	ESRL Land (ppm)	AJAX Land (ppm)
Co-location error	LMT	0.5±0.2 0.9±0.4	0.3±0.1	0.3±0.1	2.1±0.7	1.1
	U		0.1±0.1	0.2±0.0	0.5±0.3	0.1
	XCO ₂		0.1±0.2	0.2±0.1	0.8±0.3	0.2
Predicted error (n=1)	LMT	4.3±0.2	4.3±0.3	4.3±0.1	4.6±0.3	4.1
	U		1.7±0.1	1.7±0.0	1.8±0.0	1.7
	XCO ₂		0.6±0.1	0.7±0.1	0.9±0.1	0.8
GOSAT error (n=1)	LMT	1.7±0.4	1.7±0.3	1.5±0.1	3.4±0.7	2.9
	U		0.8±0.1	0.8±0.0	1.3±0.3	1.1
	XCO ₂		0.9±0.1	0.8±0.1	1.7±0.4	0.9
True variability	LMT	1.3±0.8	0.6± 0.2	0.9±0.6	5.5±2.0	2.8
	U		0.4±0.3	0.8±0.8	2.0±0.2	2.0
	XCO ₂		0.3±0.3	0.8±0.8	2.5±0.6	2.4
Prior error (n=15)	LMT	2.2±0.9	0.5± 0.3	0.7±0.2	2.1±1.0	-
	U		0.3±0.1	0.5±0.0	0.9±0.2	-
	XCO ₂		0.3±0.1	0.5±0.1	1.1±0.6	-
GOSAT error (n=15)	LMT	0.4±0.3	0.5± 0.1	0.4±0.1	1.9±1.1	-
	U		0.4±0.1	0.6±0.1	0.7±0.4	-
	XCO ₂		0.3±0.1	0.4±0.1	0.8±0.5	-

1708
1709
1710

Table 6. Estimated co-location, correlated, and random errors using Eq. 12. The co-location errors are taken from Table 4.

	Type	Ocean surface (ppm)	HIPPO Ocean (ppm)	ESRL Ocean (ppm)	ESRL Land (ppm)
Co-location error	LMT	1.0±0.4	0.3±0.1	0.3±0.1	2.1±0.7
	U		0.1±0.1	0.2±0.0	0.5±0.3
	XCO ₂		0.1±0.1	0.1±0.1	0.8±0.3
Correlated error (a_o)	LMT	0.4±0.3	0.3±0.2	0.3±0.2	1.7±1.3
	U		0.3±0.2	0.5±0.1	0.6±0.4
	XCO ₂		0.2±0.2	0.4±0.1	1.1±0.6
Random error (b)	LMT	1.6±0.4	1.6±0.3	1.4±0.2	3.0±0.6
	U		0.8±0.1	0.6±0.1	1.2±0.1
	XCO ₂		0.9±0.1	0.4±0.1	0.8±0.3

1711
1712
1713
1714

Table 7. Enhancements in CO and CO₂ for May and August, 2010. The target box is 11 to 18S, 60 to 56W for May, and 13-17S, 55-60W, for August. The CO background box is 11 to 18S, 40 to 44W for May and

1715 157.8-161.8W, 19-23S for August. Rarotonga aircraft measurements are
 1716 used for CO₂ background. The different CO target columns are for different
 1717 cutoffs for the degrees of freedom between the surface and 200 hPa above
 1718 the surface for MOPITT.

		CO					GOSAT LMT CO ₂	
		backg rnd (ppb)	Target all (ppb)	Target DOFs > 0.15) (ppb)	Target (DOFs > 0.25) (ppb)	Target (DOFs > 0.30) (ppb)	backgrn d from RTA (ppm)	Target (DOFs = 0.8) (ppm)
May, 2010	Mean	68±9	122±49	123±54	146±77	182±96	386.4	389.6±2.5
	N	1502	2023	1556	500	215		26
	DOFs		0.21	0.24	0.32	0.39		0.85
	Δvalue	-	54	55	88	114	-	3.2
	Em. ratio		6%	6%	7%	7%	-	-
August, 2010	Mean	91±22	305±171	311±180	336±200	372±221	387.4	393.1±4.8
	N	2989	3881	3227	1887	1231		49
	Δvalue (ppb)	-	213.7	219.3	244.8	281.1	-	5.7
	Em. ratio		15%	13%	11%	10%		

1719
 1720 Table 8a. Bias terms for LMT – U. Compare to Table 4.

	HIPPO Ocean (ppm)	ESRL Ocean (ppm)	ESRL Land (ppm)
Co-location bias	-0.4±0.2	-0.2±0.3	-0.6±0.5
True mean	1.1±0.8	0.4±0.5	1.0±2.7
Prior bias	-1.0±1.3	-2.8±2.9	-1.0±1.2
GOSAT bias	0.0±0.4	-0.5±0.9	-0.5±0.8

1721
 1722 Table 8b. Standard deviations for LMT – U. Compare to Table 5. The
 1723 predicted errors in the table use the errors given at the end of Section 5.1.5.

	HIPPO Ocean (ppm)	ESRL Ocean (ppm)	ESRL Land (ppm)
Co-location error	0.3±0.1	0.3±0.1	2.1±0.7
Predicted error (n=1)	1.2±0.0	1.2±0.0	2.7±0.0
GOSAT error (n=1)	1.5±0.4	1.3±0.1	2.3±0.5
true variability	0.5± 0.2	0.8±0.1	4.8±1.5
Prior error (n=15)	0.5± 0.2	0.8±0.1	1.4±0.8
GOSAT error (n=15)	0.5± 0.2	0.7±0.1	1.2±0.8

1724
 1725 Table 8c. Error fits for LMT – U. Compare to Table 6.

	HIPPO Ocean (ppm)	ESRL Ocean (ppm)	ESRL Land (ppm)
Co-location error	0.3±0.1	0.3±0.1	2.1±0.7

Correlated error (a)	0.4±0.2	0.6±0.0	0.9±0.9
Random error (b)	1.4±0.4	1.1±0.1	2.1±0.7

1726

1727 Table A.1 Filtering and Bias corrections. Note observations over land and
 1728 ocean are corrected separately.

parameter	ocean filtering	ocean bias correction	land filtering	land bias correction
albedo_2	0.0215 < val < 0.024	-1272.02 ± 50	-	-
albedo_slope_2	val < 8e-6	-	-	-
aod_dust	val < 0.01	-	-	-36.03 ± 1
aod_total	val < 0.25	-	-	-
h2o_ratio	0.96 < val < 1.02	-	-	-
co2_grad_delta	-40 < val < 17	0.396330 ± 0.004	-	0.310 ± 0.003
constant	-	52.674 ± 6	-	0.01259 ± 0.4
b1_offset	-	-1.25204 ± 0.05	-	-
surfacepressure_xa	-	-0.0381105 ± 0.006	-	-
s32	-	17.0742 ± 3	-	-
surfacepressurediff	-	0.869280 ± 0.05	-	-
albedo_1	-	144.458 ± 9	-	-
co2_grad_delta_prime	-	-0.171350 ± 0.01	-	-0.027 ± 0.005
dofs_LMT	-	-	val > 0.68	-
xco2_error	-	-	val < 1.4	6.02 ± 0.3
albedo_slope_3	-	-	-1.5e-4 < val < 2.0e-4	-
xco2_dofs	-	-	val > 1.3	-
ice_height	-	-	val > -0.1	-
surfacePressureDiff	-	-	-4 < val < 2	-
albedo_3	-	-	-	-11.66 ± 0.7
dp_cld	-	-	-	0.219 ± 0.01

1729 * parameters also used in ACOS-GOSAT XCO₂ bias correction

1730

1731 Table A2a. Effects of bias corrections and quality flags on land comparisons
 1732 (ESRL aircraft land observations)

	n	lmt bias (ppm)	lmt bias var. (ppm)	lmt stdev (ppm)	u bias var. (ppm)	u stdev (ppm)
original (XCO ₂ flags)	15143	13.54	2.79	7.70	1.61	3.05
all quality flags (see appendix A)	12714	13.37	2.30	7.55	1.27	2.98
bias correction (see appendix A)	12714	-1.18	1.43	3.47	0.79	1.36
fit U separately	11978	-	-	-	0.70	1.43

1733

1734 Table A2b. Effects of bias corrections and quality flags on ocean
 1735 comparisons (HIPPO and ESLR ocean dataset stations/campaigns: tgc, rta,
 1736 aoa, 2S, 2N, 3S, 3N, 4S, 4N, 5S, 5N)

	n	lmt bias (ppm)	lmt bias var. (ppm)	lmt stdev (ppm)	u bias var. (ppm)	u stdev (ppm)
original (XCO ₂ flags)	9836	1.73	3.46	3.77	0.78	0.85
with cutoffs (see Appendix A)	6143	1.47	1.92	3.18	0.63	0.69

bias correction (see Appendix A)	6143	0.04	0.68	1.60	0.38	0.79
fit U separately	6143	-	-	-	0.35	0.60

1737
1738 The fit parameters are tested for robustness by using a subset of the dataset
1739 to determine the fit and then testing the fit on the independent subset. For
1740 the ocean data, HIPPO campaigns 2N, 3S, 4, and 5 are used to develop bias
1741 correction, and HIPPO 2S and 3N are used for testing. For land data,
1742 stations bne, car, cma, dnd, esp, etl, hil, hip, are used for development, and
1743 stations lef, nha, pfa, sca, sgp, tgc, thd, wbi are used for testing.

1744
1745 Table A3a: Bias correction robustness test for LMT observations over ocean.
1746 Comparisons to aircraft data are tested using (a) no bias correction, (b) bias
1747 correction using the test dataset, (c) an independent dataset, and (d) the
1748 entire dataset

Bias correction testing	Mean bias	Bias std	mean std
no correction	0.69	0.69	2.97
subset tested on itself	-0.04	0.33	1.47
independent subset	-0.26	0.46	1.58
all data used	-0.14	0.49	1.54

1749
1750 Table A3b: Bias correction robustness test for LMT observations over land.
1751 Same as Table A3a but for land.

Bias correction testing	Mean bias	Bias std	mean std
no correction	13.00	2.47	7.54
subset tested on itself	0.16	1.55	3.68
independent subset	1.05	1.24	3.67
all data used	0.50	1.51	3.65

1752
1753 Table A4: Effect of profile extension. GOSAT corrected as described in
1754 Table A1 and compared to aircraft data with profile extended 4 different
1755 ways: (a) using the GOSAT prior, (b) extending the aircraft to the
1756 tropopause pressure, with the GOSAT prior above this, (c) using the CT2015
1757 model, and (d) extending the aircraft to the tropopause pressure, with the
1758 CT2015 above this

Profile extension	LMT bias	LMT Bias std	LMT std	U bias	U Bias std	U std
(a) prior	-0.90	1.37	3.46	-0.38	0.70	1.25
(b) extend+prior	-0.99	1.44	3.47	-0.20	0.79	1.35
(c) CT2015	-1.20	1.39	3.47	-0.02	0.66	1.26
(d) extend+CT2015	-1.18	1.43	3.47	-0.05	0.79	1.36

1759
1760 Table A5: Effect of profile extension, part 2. Extension of the aircraft with
1761 CarbonTracker versus extension with AirCore

Profile extension	LMT bias	LMT std	U bias	U std
(a) CT2015	0.3	3.1	-0.2	1.0
(b) AirCore	0.0	3.1	0.2	1.0

1762
1763
1764
1765
1766

Table B1. Actual and predictions of errors by station/campaign. See Table 3 for definitions of the quantities calculated in Table B1.

location	latitude, longitude	Co-location error	<i>a</i> corr. error	<i>b</i> rand. error	GOSAT prior bias (n=1)	GOSAT error (n=1)	pred. Error (n=1)	Co-location bias	true mean	prior bias	GOSAT bias	true stdev (n=1)	prior error (n=15)	GOSAT error (n=15)
		(ppm)	(ppm)	(ppm)	(ppm)	(ppm)	(ppm)	(ppm)	(ppm)	(ppm)	(ppm)	(ppm)	(ppm)	(ppm)
a) LMT vs. surface ocean flasks at remote sites														
BMW	32N,65W	0.4	0.9	2.5	4.6	2.6	4.2	-0.8	391.8	-3.0	-1.4	3.3	2.8	1.1
MID	28N,177W	0.8	1.5	1.8	4.2	2.3	4.3	0.1	389.9	-2.4	-0.2	2.2	4.5	1.5
MNM	24N,154E	0.3	0.8	1.6	3.8	1.8	4.2	0.2	393.2	-3.8	-0.6	1.6	2.8	0.9
MLO	20N,156W	0.8	1.0	1.4	2.6	1.7	4.5	-0.6	390.9	-2.1	-0.3	1.7	2.2	1.0
KUM	20N,155W	0.7	1.5	1.2	2.6	1.9	4.5	-0.6	390.0	-1.1	0.7	1.7	2.5	1.5
GMI	13N,145E	0.5	0.7	1.6	2.8	1.8	4.4	0.0	394.8	-2.9	0.9	1.2	1.9	0.8
CHR	2N,157W	0.3	0.8	1.4	1.6	1.6	4.4	-0.2	392.1	-0.8	0.4	1.1	1.9	0.9
SEY	5S,56E	0.4	1.3	1.8	2.2	2.2	4.0	-0.3	391.4	-0.2	0.7	1.3	0.8	1.3
ASC	8S,14W	0.3	1.0	1.5	1.7	1.8	4.4	-0.4	390.4	0.1	1.5	0.7	2.5	1.1
SMO	14S,171W	0.5	0.5	1.7	2.2	1.8	4.2	-0.5	390.6	0.0	0.6	0.5	2.2	0.7
EIC	27S,109W	0.5	0.8	1.2	2.1	1.4	4.2	-0.4	389.7	0.7	2.7	0.7	1.9	0.8
average		0.5	1.0	1.5	2.6	1.8	4.3	-0.3	391.3	-1.2	0.7	1.3	2.3	1.1
		±0.2	±0.3	±0.2	±0.8	±0.3	±0.2	±0.3	±1.6	±1.5	±1.0	±0.5	±0.9	±0.3
b) LMT vs. ESRL aircraft														
PFA	66N,147W	1.6	5.0	1.6	2.1	5.3	5.1	0.1	388.0	1.9	0.3	8.2	1.5	5.0
ETL	54N,105W	2.2	2.6	2.6	3.6	3.7	4.8	-0.3	388.7	-1.0	-0.6	6.9	3.5	2.7
ESP	49N,126W	3.2	3.2	4.6	4.1	5.6	5.0	0.0	386.1	-2.4	-0.2	4.4	3.6	3.4
DND	47N,99W	1.4	2.9	2.4	3.8	3.8	4.5	-0.1	390.0	-0.6	-0.7	7.8	5.0	3.0
LEF	46N,90W	2.6	3.5	2.2	3.7	4.1	4.7	-0.3	392.1	-0.9	-1.4	6.8	4.5	3.5
NHA	43N,71W	1.6	1.9	3.5	2.8	4.0	4.8	-0.3	393.3	-0.1	0.1	7.7	2.6	2.1
WBI	42N,91W	2.8	1.9	2.9	2.6	3.5	4.5	-1.5	393.3	-0.7	-0.9	5.1	2.3	2.1
THD	41N,124W	2.2	2.7	3.5	2.5	4.4	4.6	0.3	389.5	-1.5	0.9	3.9	2.5	2.8
BNE	41N,97W	2.1	2.4	3.0	3.3	3.9	4.4	-1.3	393.2	-2.5	-2.2	5.0	3.1	2.5
CAR	41N,104W	2.7	2.7	3.3	3.6	4.2	4.2	-2.2	393.0	-2.7	-2.6	3.5	3.3	2.8
HIL	40N,88W	2.2	2.2	3.0	3.4	3.8	4.5	-0.9	396.3	-2.0	-2.4	5.7	3.1	2.4
CMA	39N,74W	1.8	1.8	3.7	3.0	4.1	4.8	-0.6	394.9	-0.7	-0.5	6.1	2.3	2.0
SGP	37N,98W	1.8	2.7	2.9	4.1	3.9	4.3	-0.5	394.3	-1.5	-0.7	4.2	3.7	2.8
SCA	33N,79W	1.0	1.1	3.2	2.3	3.3	4.8	-0.5	395.6	0.3	-1.3	2.9	1.8	1.3
AOA	29N,148E	0.4	0.7	1.2	1.1	1.4	4.2	-0.5	392.4	-5.0	-0.8	1.5	0.9	0.8
TGC	28N,97W	1.1	1.5	2.5	2.7	2.9	4.2	-0.1	394.9	-0.2	0.0	2.7	2.3	1.7
RTA	21S,160W	0.4	0.2	1.6	1.0	1.6	4.3	0.0	390.9	1.3	0.7	0.7	0.7	0.5
average		2.0	2.5	3.0	3.2	4.0	4.6	-0.5	392.2	-1.0	-0.8	5.4	3.0	2.7
land		±0.6	±1.2	±0.7	±0.6	±0.7	±0.3	±0.7	±3.1	±1.2	±1.0	±1.8	±1.0	±0.9
ave. land, corrected			1.5		2.4	3.4				-0.5	-0.3		2.2	1.7
			±1.2		±0.6	±0.7				±0.1	±1.0		±1.0	±0.9
AOA, RTA	average	0.4	0.4	1.4	1.1	1.5	4.3	-0.3	391.7	-1.9	-0.1	1.1	0.8	0.7
	ocean	±0.0	±0.5	±0.3	±0.1	±0.1	±0.1	±0.4	±1.1	±0.4	±1.1	±0.6	±0.1	±0.2
c) U vs. ESRL aircraft														
PFA	66N,147W	0.5	1.3	1.1	1.3	1.7	1.8	0.1	392.0	1.8	1.5	2.4	1.0	1.3
ETL	54N,105W	0.4	1.0	1.2	1.6	1.6	1.8	0.1	390.8	1.3	0.9	1.8	1.7	1.1
ESP	49N,126W	1.2	2.0	1.1	1.6	2.3	1.8	0.4	389.9	1.7	2.2	2.1	1.9	2.0
DND	47N,99W	0.6	0.7	1.3	1.6	1.5	1.8	0.2	390.5	0.8	0.4	2.2	1.8	0.8
LEF	46N,90W	0.5	0.5	1.2	1.4	1.3	1.8	0.0	391.3	0.4	0.1	2.1	1.5	0.6
NHA	43N,71W	0.5	0.8	1.2	1.3	1.5	1.8	0.0	391.5	0.4	0.3	2.5	0.9	0.8
WBI	42N,91W	0.4	0.6	1.1	0.8	1.2	1.8	-0.2	391.2	0.3	-0.2	2.1	0.6	0.7
THD	41N,124W	0.9	1.0	1.2	1.2	1.6	1.8	0.4	390.5	1.4	1.8	1.9	0.8	1.1

BNE	41N,97W	0.4	0.6	1.2	1.1	1.3	1.7	-0.1	391.2	0.4	-0.4	2.0	1.1	0.7
CAR	41N,104W	0.6	0.8	1.3	1.0	1.5	1.7	-0.2	391.1	0.4	0.0	2.0	1.0	0.8
HIL	40N,88W	0.5	0.7	1.1	1.1	1.3	1.8	-0.1	392.1	-0.4	-0.9	2.0	0.9	0.8
CMA	39N,74W	0.3	0.5	1.4	0.9	1.5	1.8	-0.1	391.5	0.3	0.1	2.1	0.5	0.6
SGP	37N,98W	0.4	0.5	1.1	0.8	1.2	1.7	0.0	391.4	0.0	-0.4	1.7	0.7	0.6
SCA	33N,79W	0.2	0.4	1.1	0.5	1.2	1.8	-0.1	391.8	0.2	-0.8	1.6	0.3	0.5
AOA	29N,148E	0.2	0.6	0.4	0.5	0.8	1.7	-0.1	392.4	0.0	0.6	1.4	0.5	0.6
TGC	28N,97W	0.2	0.3	1.0	0.5	1.1	1.7	0.0	391.6	0.4	-0.3	1.9	0.5	0.4
RTA	21S,160W	0.2	0.5	0.7	0.5	0.8	1.7	0.0	390.1	2.3	0.8	0.2	0.5	0.5
average land		0.5	0.7	1.2	1.1	1.4	1.8	0.0	391.2	0.6	0.3	2.0	1.0	0.8
		±0.3	±0.4	±0.1	±0.4	±0.3	±0.0	±0.2	±0.6	±0.6	±0.9	±0.2	±0.2	±0.4
ave. land, corrected			0.6		0.5	1.3				0.6	0.3	2.0	0.9	0.5
			±0.4		±0.0	±0.3				±0.6	±0.9	±0.2	±0.2	±0.4
AOA, RTA	average ocean	0.2	0.6	0.6	1.0	0.8	1.7	-0.1	391.3	-1.2	0.7	0.8	0.5	0.6
		±0.0	±0.1	±0.2	±0.4	±0.0	±0.0	±0.1	±1.6	±1.6	±0.1	±0.8	±0.0	±0.1

d) XCO₂ vs. ESRL aircraft

PFA	66N,147W	0.7	2.1	1.2	1.4	2.4	1.3	0.2	391.1	1.8	1.2	3.8	1.0	2.1
ETL	54N,105W	0.7	1.3	1.5	1.9	2.0	0.9	0.0	390.3	0.7	0.6	2.8	2.1	1.4
ESP	49N,126W	1.5	2.2	2.0	1.9	2.9	0.9	0.4	389.0	0.8	1.6	2.4	2.1	2.2
DND	47N,99W	0.7	1.0	1.6	2.0	1.9	0.9	0.1	390.4	0.5	0.2	3.1	2.4	1.1
LEF	46N,90W	0.9	1.1	1.5	1.7	1.8	1.0	0.0	391.4	0.1	-0.3	2.7	2.0	1.2
NHA	43N,71W	0.7	0.9	1.7	1.5	1.9	1.0	-0.1	391.9	0.3	0.3	3.5	1.2	1.0
WBI	42N,91W	0.9	0.8	1.4	1.0	1.6	0.8	-0.5	391.7	0.0	-0.3	2.3	0.8	0.9
THD	41N,124W	1.1	1.2	1.7	1.1	2.1	0.9	0.4	390.3	0.7	1.6	2.2	1.0	1.3
BNE	41N,97W	0.6	0.8	1.5	1.2	1.7	0.7	-0.4	391.7	-0.3	-0.8	2.2	1.3	0.9
CAR	41N,104W	1.0	1.0	1.7	1.1	2.0	0.8	-0.6	391.5	-0.3	-0.7	2.1	1.2	1.1
HIL	40N,88W	0.8	1.0	1.5	1.6	1.8	0.9	-0.3	393.1	-0.7	-1.3	2.4	1.3	1.0
CMA	39N,74W	0.6	0.6	1.9	1.2	2.0	0.9	-0.2	392.3	0.0	0.0	2.8	0.8	0.8
SGP	37N,98W	0.7	0.9	1.4	1.2	1.7	0.8	-0.1	392.1	-0.3	-0.5	1.9	1.1	1.0
SCA	33N,79W	0.3	0.3	1.5	0.7	1.6	0.9	-0.2	392.7	0.2	-0.9	1.7	0.6	0.5
AOA	29N,148E	0.2	0.5	0.6	0.5	0.8	0.6	-0.2	392.4	-1.2	0.3	1.4	0.5	0.6
TGC	28N,97W	0.4	0.5	1.2	0.9	1.4	0.7	0.0	392.3	0.3	-0.3	1.9	0.9	0.6
RTA	21S,160W	0.1	0.3	0.8	0.5	0.9	0.7	0.0	390.3	2.0	0.8	0.2	0.4	0.4
average land		0.8	1.0	1.6	1.5	1.9	0.9	-0.1	391.5	-0.3	-0.0	2.5	1.3	1.1
		±0.3	±0.5	±0.2	±0.4	±0.4	±0.1	±0.3	±1.1	±0.6	±0.9	±0.6	±0.6	±0.5
ave. land, corrected			0.7		0.5	1.7				-0.2	0.1		1.1±0.6	0.6
			±0.5		±0.0	±0.4				±0.6	±0.9			±0.5
AOA, RTA	average ocean	0.2	0.4	0.7	1.1	0.9	0.7	-0.1	391.4	0.4	0.6	0.8	0.5	0.5
		±0.1	±0.1	±0.1	±0.4	±0.1	±0.1	±0.1	±1.5	±2.3	±0.4	±0.8	±0.1	±0.1

e) LMT GOSAT HIPPO ocean

2S	30S-0S	0.3	0.3	1.5	0.5	1.5	4.0	-0.1	390.9	2.0	-0.4	0.5	0.4	0.5
2N	15S-5S	0.4	0.3	1.6	0.5	1.6	4.1	-0.1	390.7	2.2	-0.2	0.4	0.5	0.5
3S	10S-10N	0.2	0.0	2.4	0.7	2.4	4.3	-0.4	393.5	-0.1	0.0	1.2	0.3	0.6
3N	5S-10N	0.5	0.3	1.9	0.5	1.9	3.9	-0.4	393.4	-0.1	-0.4	0.6	0.4	0.6
4S	10N	0.1	0.5	1.5	0.5	1.6	4.6	-0.5	394.5	-3.0	0.2	0.3	0.4	0.6
4N	15-30N	0.3	0.4	1.5	1.2	1.5	4.2	-0.3	393.4	-4.2	-0.5	0.5	0.8	0.5
5S	0-20N	0.4	0.6	1.5	1.4	1.6	4.5	-0.2	390.7	-0.1	-0.4	0.6	1.0	0.7
5N	10S-20N	0.5	0.5	1.3	1.1	1.4	4.5	-0.3	390.6	2.0	0.3	0.7	0.8	0.6
average		0.3	0.4	1.6	0.8	1.7	4.3	-0.3	392.2	-0.2	-0.2	0.6	0.6	0.6
		±0.1	±0.2	±0.3	±0.4	±0.3	±0.3	±0.2	±1.6	±2.4	±0.3	±0.3	±0.3	±0.6

f) U GOSAT HIPPO ocean

2S	30S-0S	0.1	0.6	0.8	0.4	1.0	1.6	0.1	390	2.6	0.1	0.3	0.4	0.7
2N	15S-5S	0.2	0.2	0.7	0.2	0.7	1.6	0.1	390.1	2.6	0.7	0.2	0.2	0.2
3S	10S-10N	0.1	0.3	0.9	0.6	1.0	1.7	0.0	391.6	0.9	0.3	1.0	0.6	0.4
3N	5S-10N	0.3	0.1	0.8	0.4	0.8	1.6	0.1	391.1	1.3	0.4	0.4	0.3	0.2
4S	10N	0.1	0.2	0.8	0.2	0.8	1.8	0.3	392.8	-0.2	0.2	0.2	0.2	0.3
4N	15-30N	0.1	0.2	0.7	0.3	0.7	1.6	-0.1	392.9	-0.3	0.2	0.2	0.2	0.3
5S	0-20N	0.1	0.3	0.8	0.3	0.9	1.8	0.1	390.4	1.2	-0.2	0.2	0.2	0.4
5N	10S-20N	0.2	0.3	0.7	0.3	0.8	1.8	0.1	390.2	1.8	0.0	0.3	0.2	0.4
average		0.1	0.3	0.8	0.3	0.8	1.7	0.1	391.1	0.3	0.2	0.4	0.3	0.4
		±0.1	±0.2	±0.1	±0.1	±0.1	±0.1	±0.1	±1.2	±1.1	±0.3	±0.3	±0.1	±0.1

g) XCO₂ GOSAT HIPPO ocean

2S	30S-0S	0.1	0.4	0.8	0.2	0.9	0.5	0.0	390.2	2.5	0.0	0.2	0.2	0.5
2N	15S-5S	0.1	0.0	0.7	0.2	0.7	0.5	0.0	390.2	2.5	0.5	0.2	0.2	0.2

3S	10S-10N	0.1	0.2	1.1	0.6	1.1	0.7	-0.1	392.0	0.6	0.2	1.1	0.5	0.3
3N	5S-10N	0.3	0.0	0.9	0.4	0.9	0.5	0.0	391.6	1.0	0.2	0.5	0.2	0.2
4S	10N	0.1	0.3	0.9	0.2	0.9	0.8	0.1	393.2	-0.9	0.2	0.2	0.2	0.4
4N	15-30N	0.1	0.1	0.7	0.3	0.8	0.6	-0.1	393.1	-1.2	0.0	0.2	0.1	0.2
5S	0-20N	0.1	0.3	0.9	0.5	1.0	0.7	0.0	390.5	0.9	-0.2	0.3	0.3	0.4
5N	10S-20N	0.2	0.3	0.8	0.5	0.8	0.8	0.0	390.3	1.8	0.0	0.3	0.3	0.4
average		0.1	0.2	0.9	0.4	0.9	0.6	0.0	391.4	0.9	0.1	0.4	0.3	0.3
		±0.2	±0.2	±0.1	±0.2	±0.1	±0.1	±0.1	±1.3	±1.4	±0.2	±0.3	±0.1	±0.1

h) AJAX

LMT	1.1	2.2	3.1	4.1	-0.6	393.6	-2.0	-0.2	2.8		
LMT, corrected*		1.9	2.9				-1.4	+0.4			
U	0.1	0.9	1.1	1.7	0.0	392.2	0.4	1.0	2.0		
XCO ₂	0.2	0.6	0.9	0.8	-0.1	392.4	-0.1	0.7	2.4	-	-

1767 *AJAX profiles are co-located within 1 hour and 1 degree and therefore do not have multiple GOSAT
1768 matches to average.
1769
1770

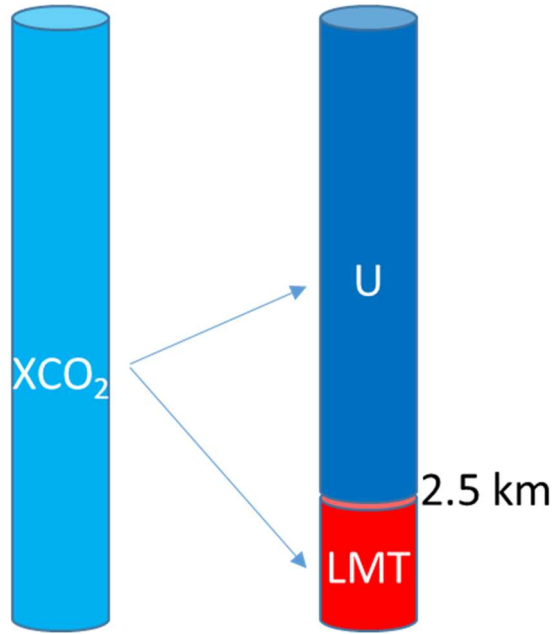


Figure 1. XCO₂ full column measurement (left) and the two partial columns that we introduce (right): the lowermost troposphere (LMT), a partial column from the surface to approximately 2.5 km, and the partial column above 2.5 km (U).

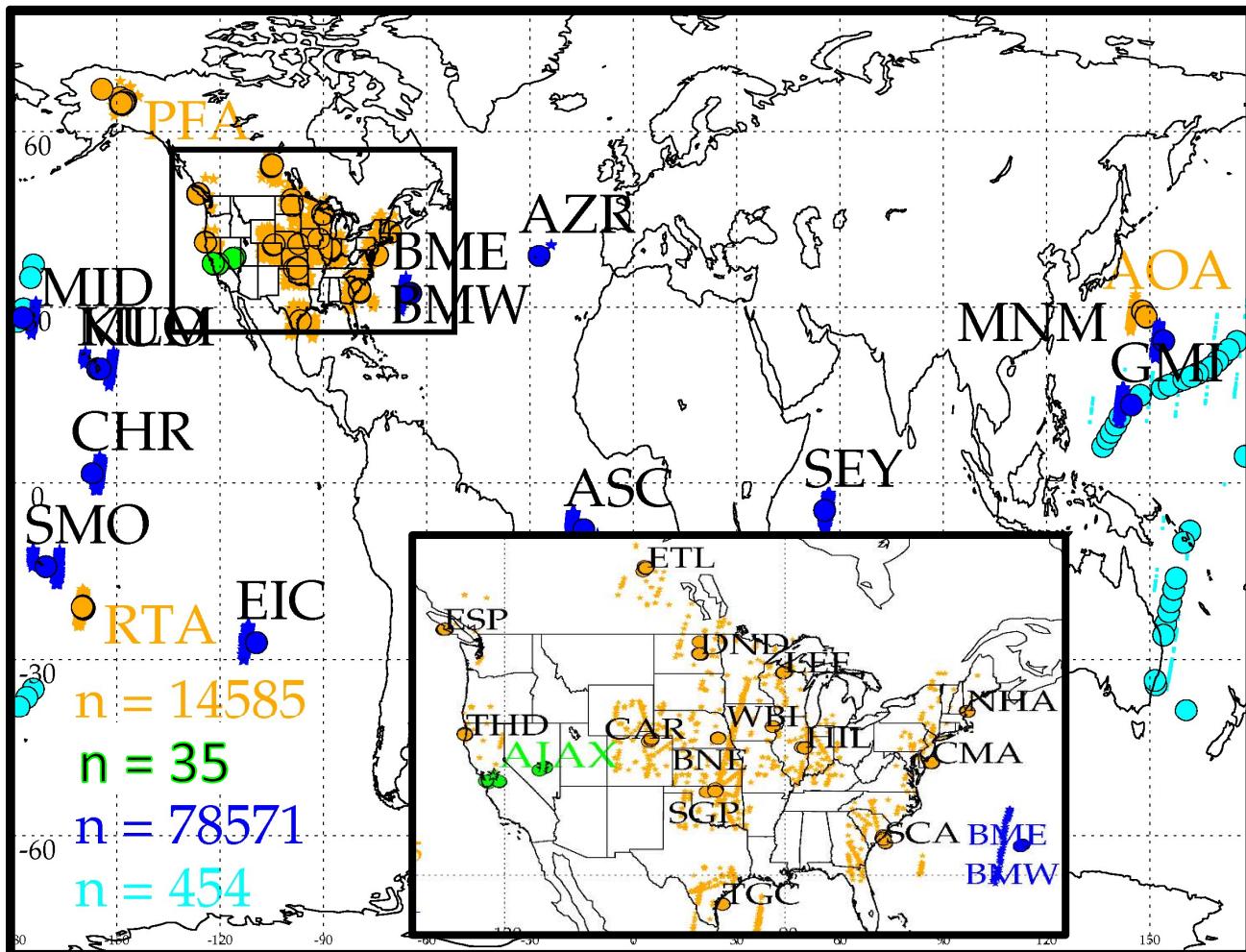


Figure 2. Validation locations. The 4 sets of validation data shown here are: ESRL aircraft profiles (orange), which occur over land (in the US) and ocean (RTA, Rarotonga, and AOA), AJAX aircraft data (green) in the western U.S., the HIPPO aircraft profiles (light blue), and remote ocean surface sites (dark blue). The matching GOSAT locations are shown as stars and the validation locations are shown as outlined circles. The number of GOSAT observations in each set are shown as the "n =" number in the lower left of the plot.

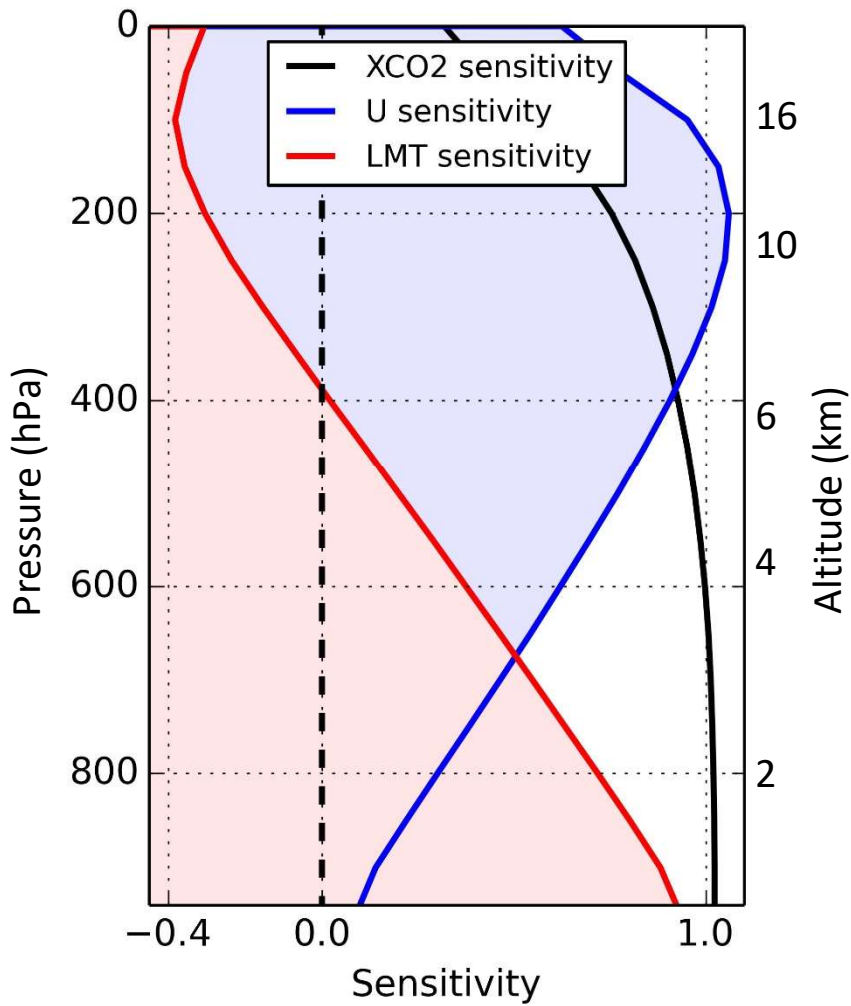


Figure 3. Sensitivity of XCO₂ (black), partitioned into the LMT (red) and U (blue) partial columns for an average land averaging kernel. The LMT sensitivity is approximately 1 near the surface and drops off steadily with decreasing pressure.

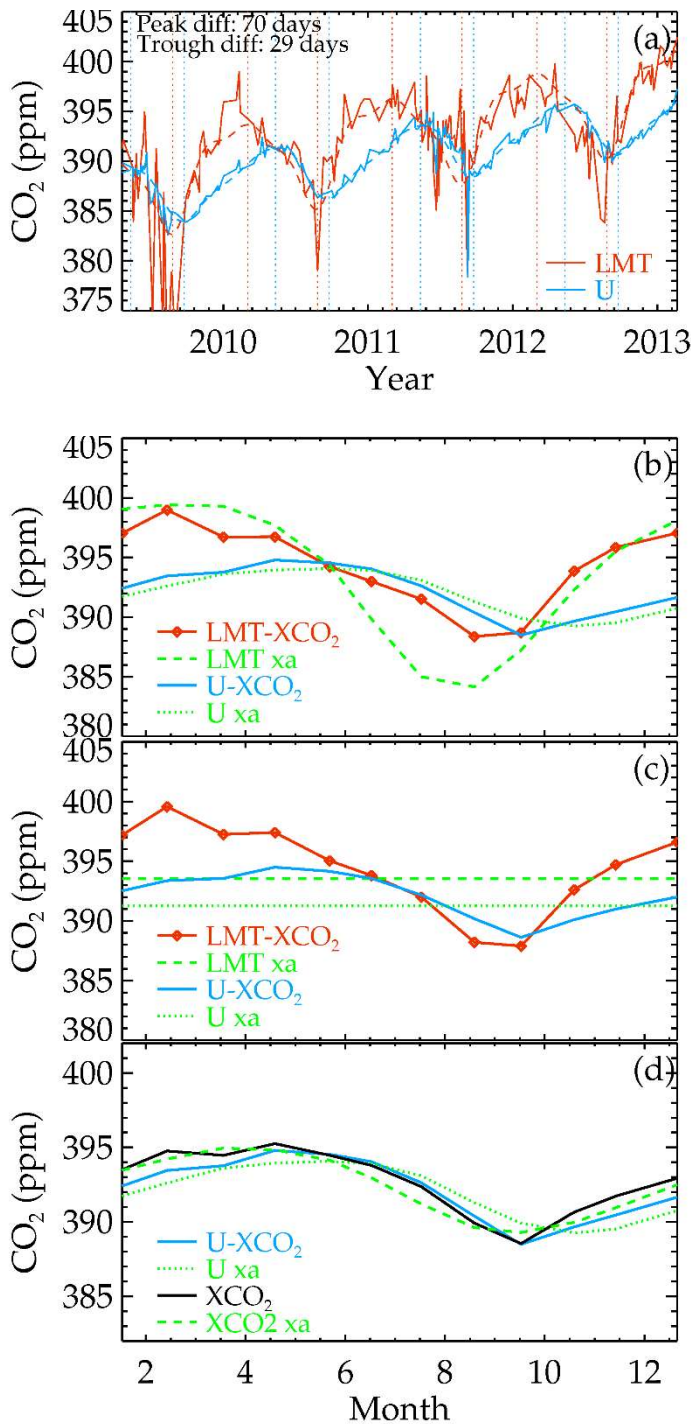


Figure 4. Simulated GOSAT retrievals from SGP aircraft profiles, Eqs. 5-6, and the GOSAT averaging kernels. (a) Time series of LMT (red) and U (blue) with monthly averages of LMT (red dashed) and U (blue dashed); (b) seasonal cycle, averaging in 1-month increments. Green dotted and dashed lines are the initial guess/a priori (xa). (c) same as (b) except that the prior is set to a constant, showing that LMT and U results are not strongly influenced by the prior. (d) Same as (b) but showing U (blue) and XCO₂ (black).

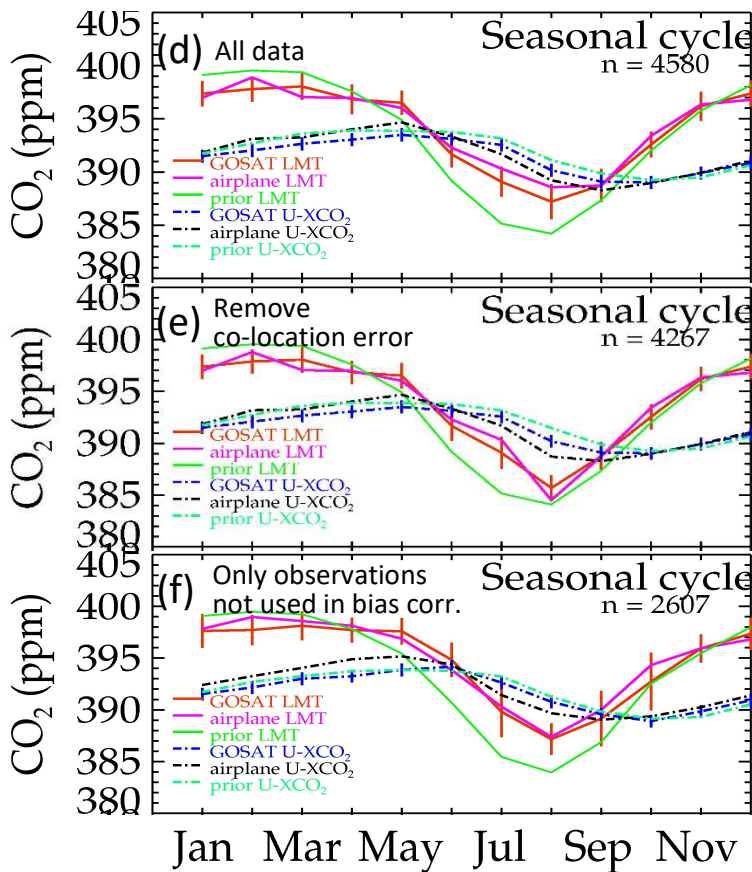
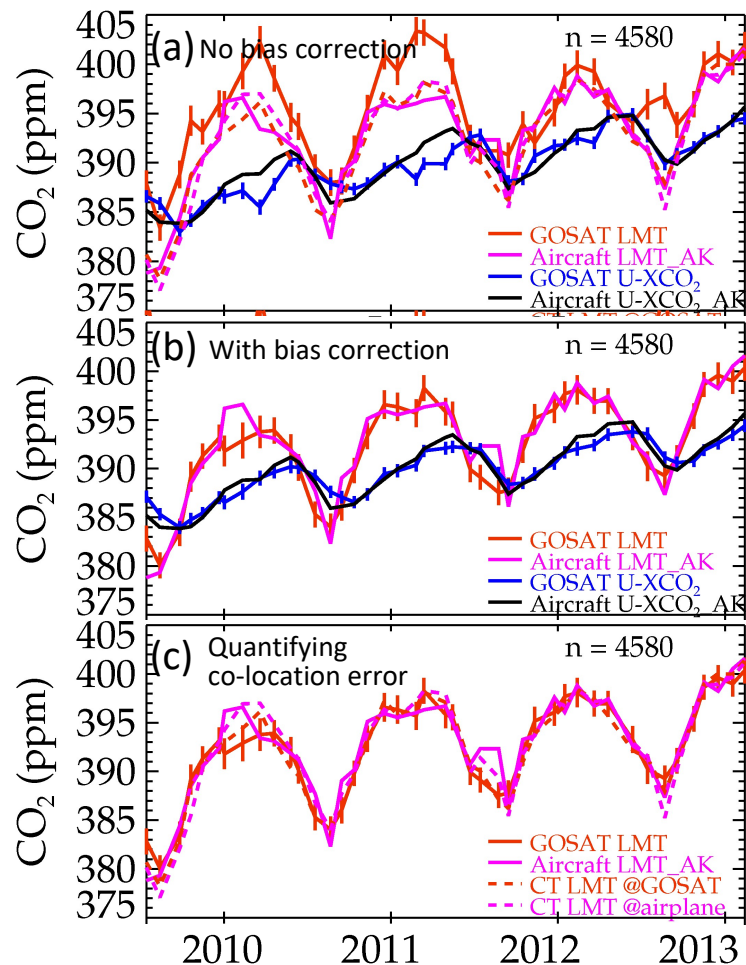


Figure 5. GOSAT versus aircraft data at the SGP site (37N, 95W). (a,b,c) Aircraft LMT (pink) and U (blue) versus GOSAT LMT (red) and U (black) for monthly averages of GOSAT/airplane matches. (a) using no bias correction, (b) using bias correction factors derived in Appendix A (c) also showing CarbonTracker matched to GOSAT (red dotted) and CarbonTracker matched to aircraft (pink dotted) for LMT. (d) Seasonal cycle of GOSAT and airplane, same colors as top panels, and adding the priors in green. (e) Seasonal cycle, but removing months where the CarbonTracker differences seen in (b) are larger than 2.5 ppm. (f) Same as (e) but with observations used in the bias correction removed from the comparison

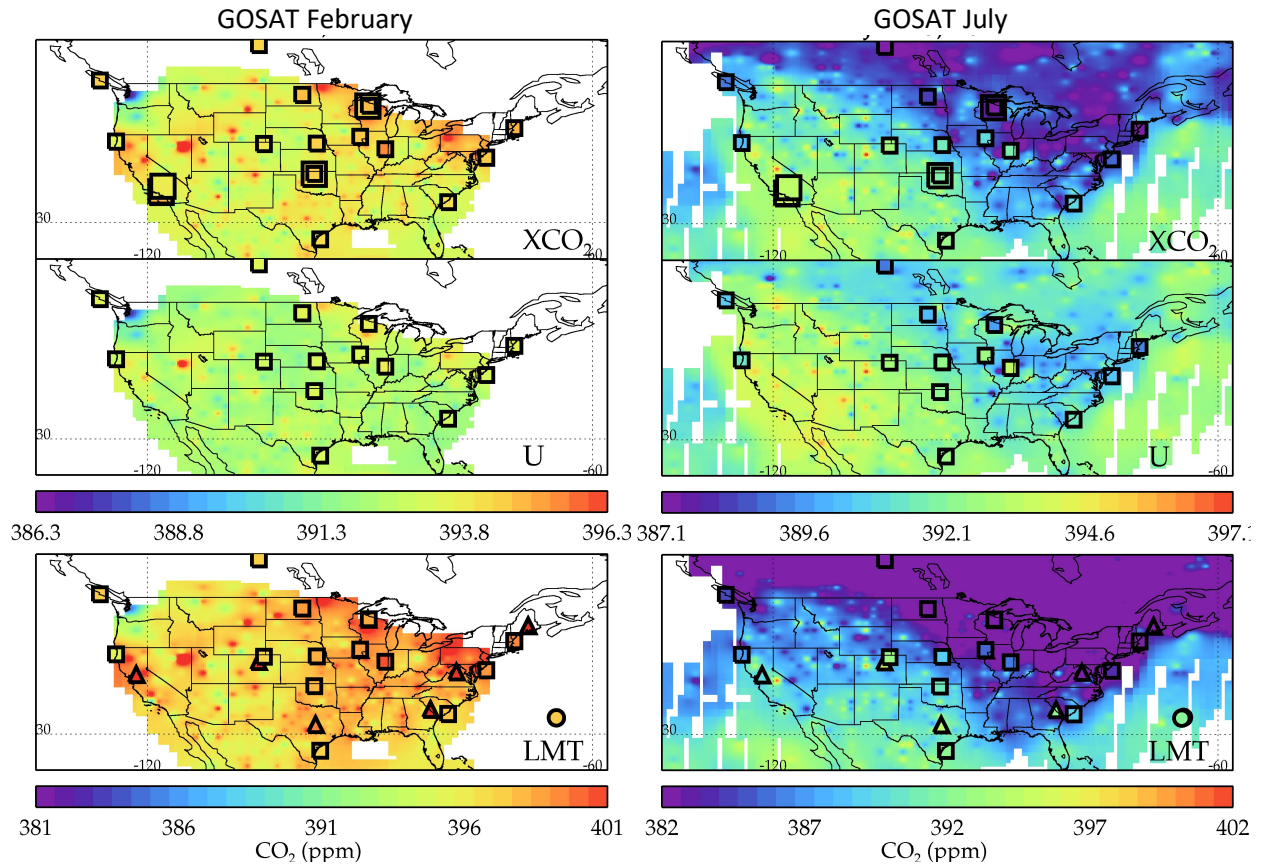


Figure 6. GOSAT XCO₂ (top), U (middle), and LMT (bottom) in February (left) and July (right). Aircraft with GOSAT averaging kernels are small squares, towers are triangles, remote ocean surface sites are circles, and TCCON are large squares (only shown on XCO₂ panels). Data is averaged over the GOSAT record.

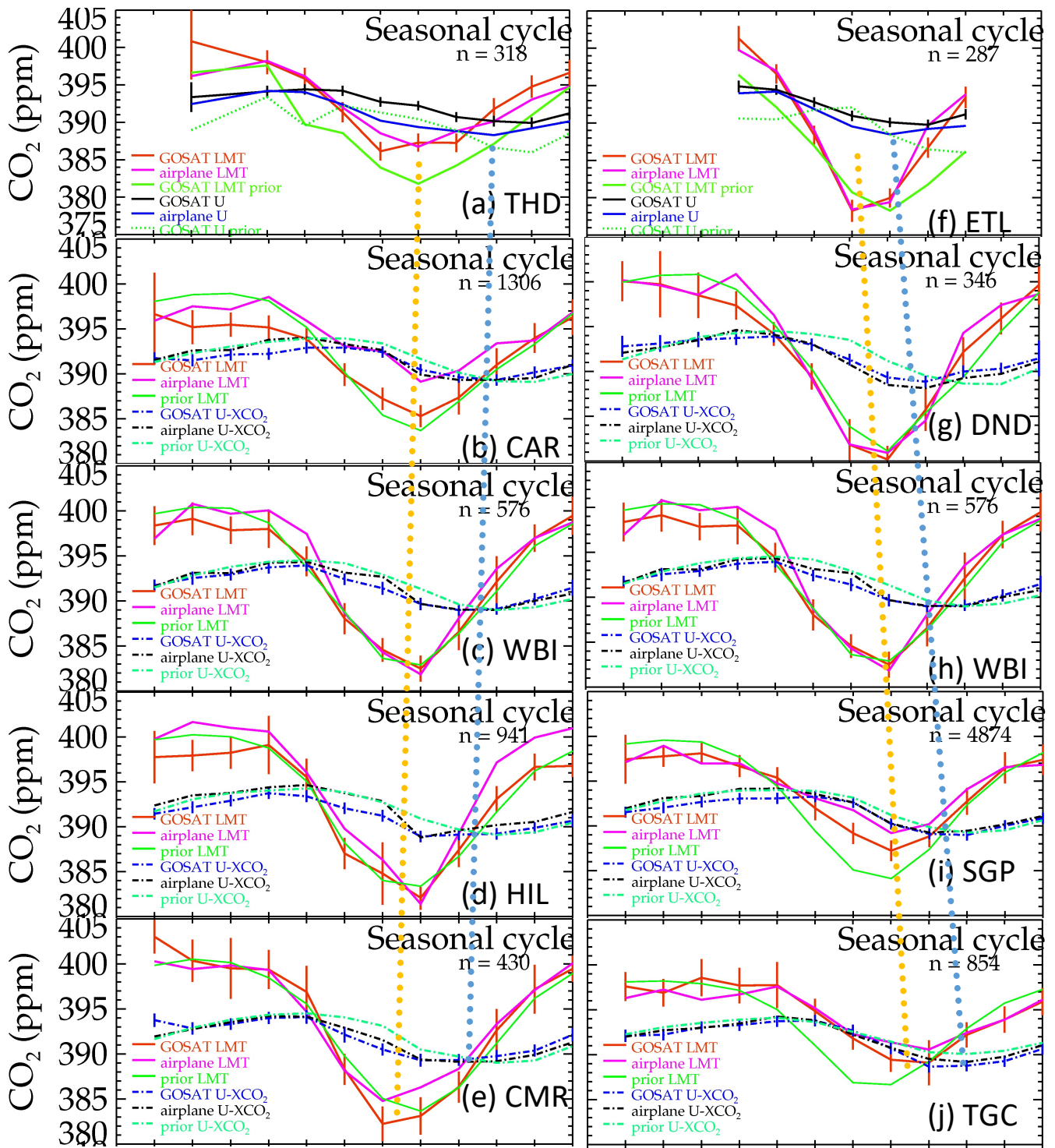


Figure 7. Seasonal cycle at 5 sites arranged from west to east (a-e) and north to south (f-j), for GOSAT LMT (red), aircraft LMT (pink), GOSAT LMT prior (green), GOSAT U (blue dashed), aircraft U (black dashed) and GOSAT U prior (green dashed). The seasonal cycle minimum is marked for LMT (orange dotted) and U (blue dotted).

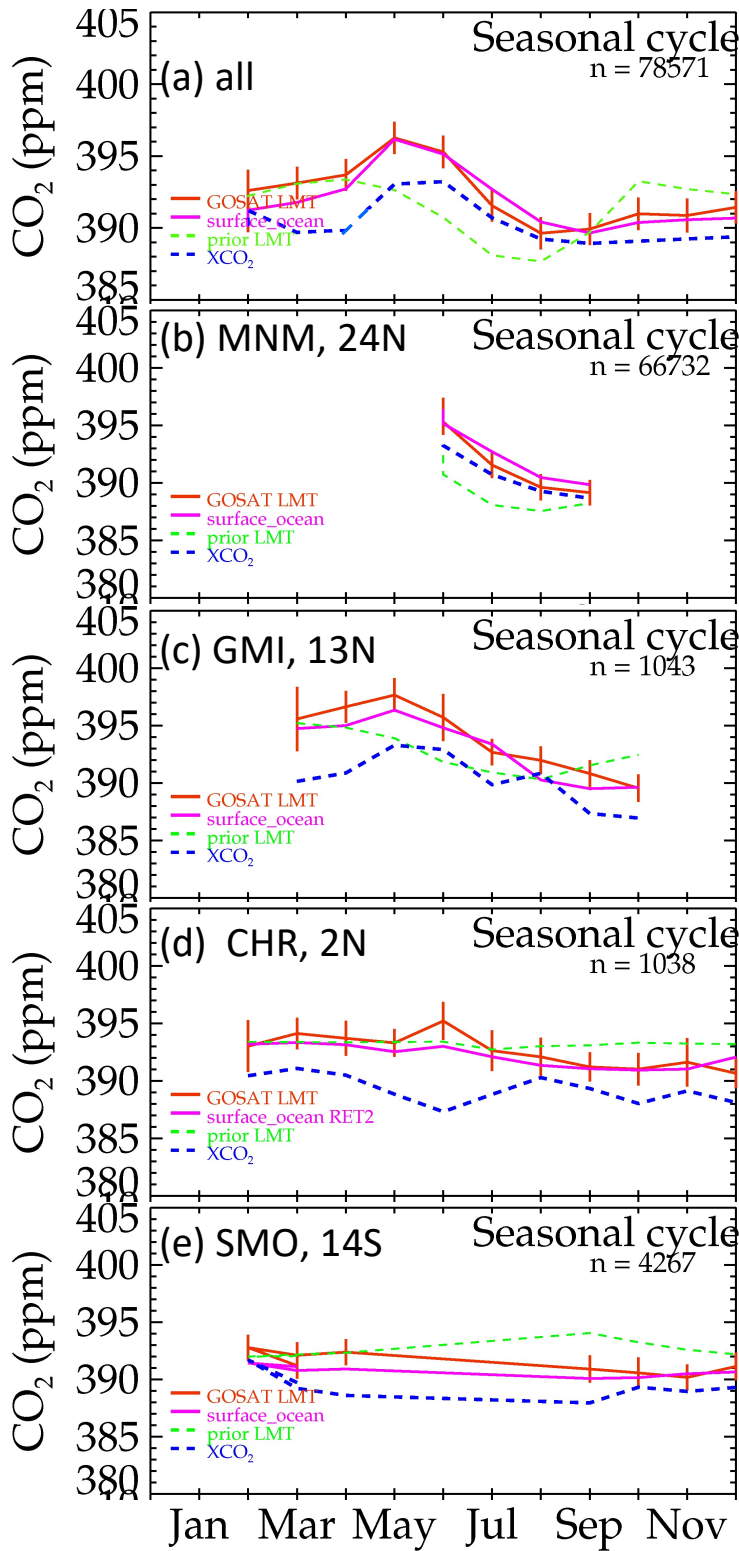


Figure 8. GOSAT LMT compared with remote ocean surface sites. GOSAT (red) improves over the prior (green dashed) versus surface sites (pink) for the average over all sites (a) and at the four sites with the most matches (b-e). XCO₂ values are shown for comparison (blue dashed).

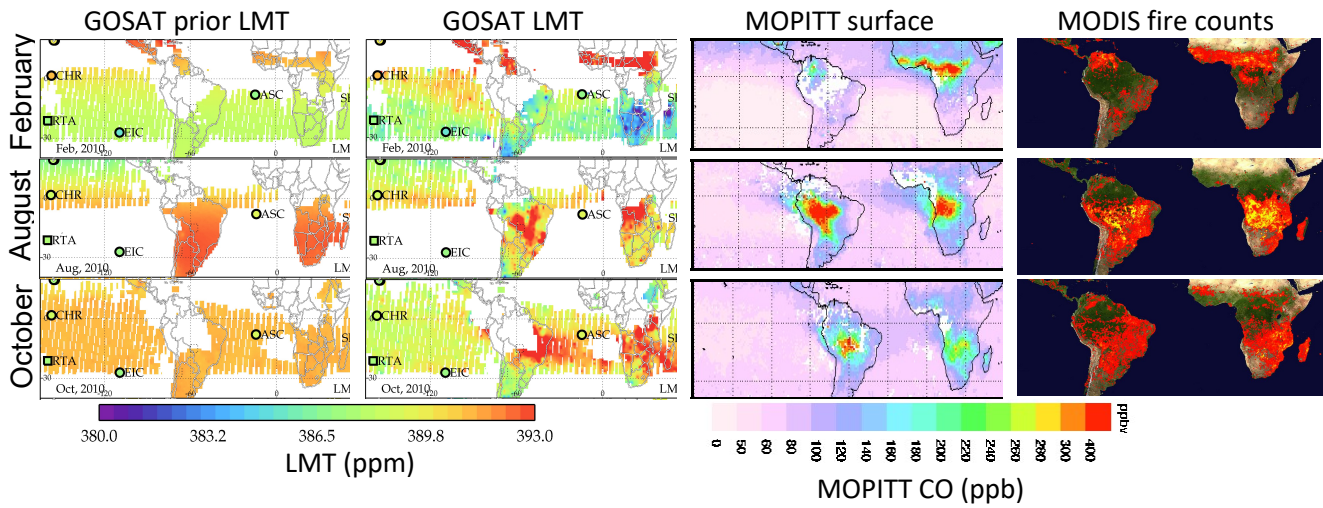


Figure 9. GOSAT LMT versus MOPITT and MODIS fire counts in for February, August, and October, 2010. GOSAT prior (left) and retrieved (second column) LMT compared with MOPITT multispectral CO (third column) and MODIS fire counts (right).

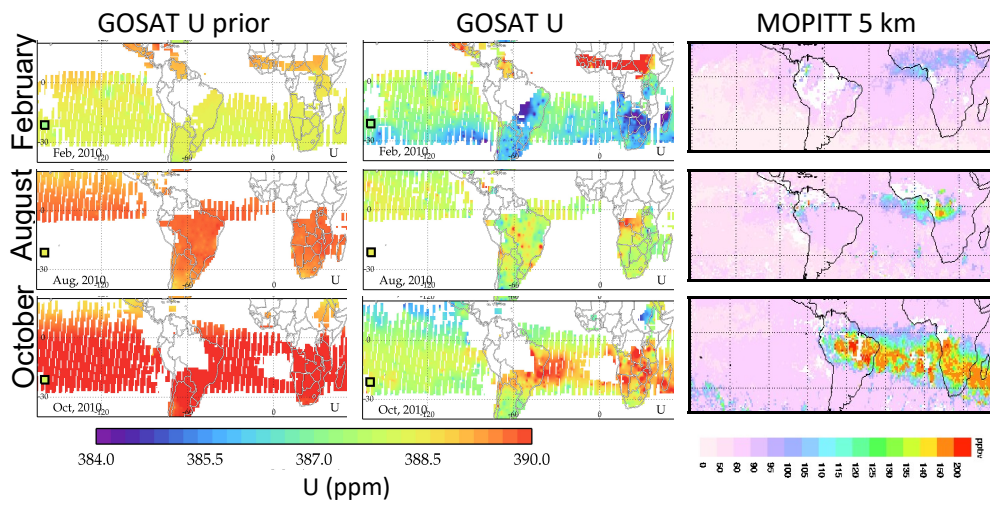


Figure 10. GOSAT U versus MOPITT for February, August, and October, 2010. GOSAT prior (left) and retrieved (middle) compared with MOPITT multispectral CO (right) at 5 km. Note the biomass burning outflow see in October for both MOPITT and GOSAT.

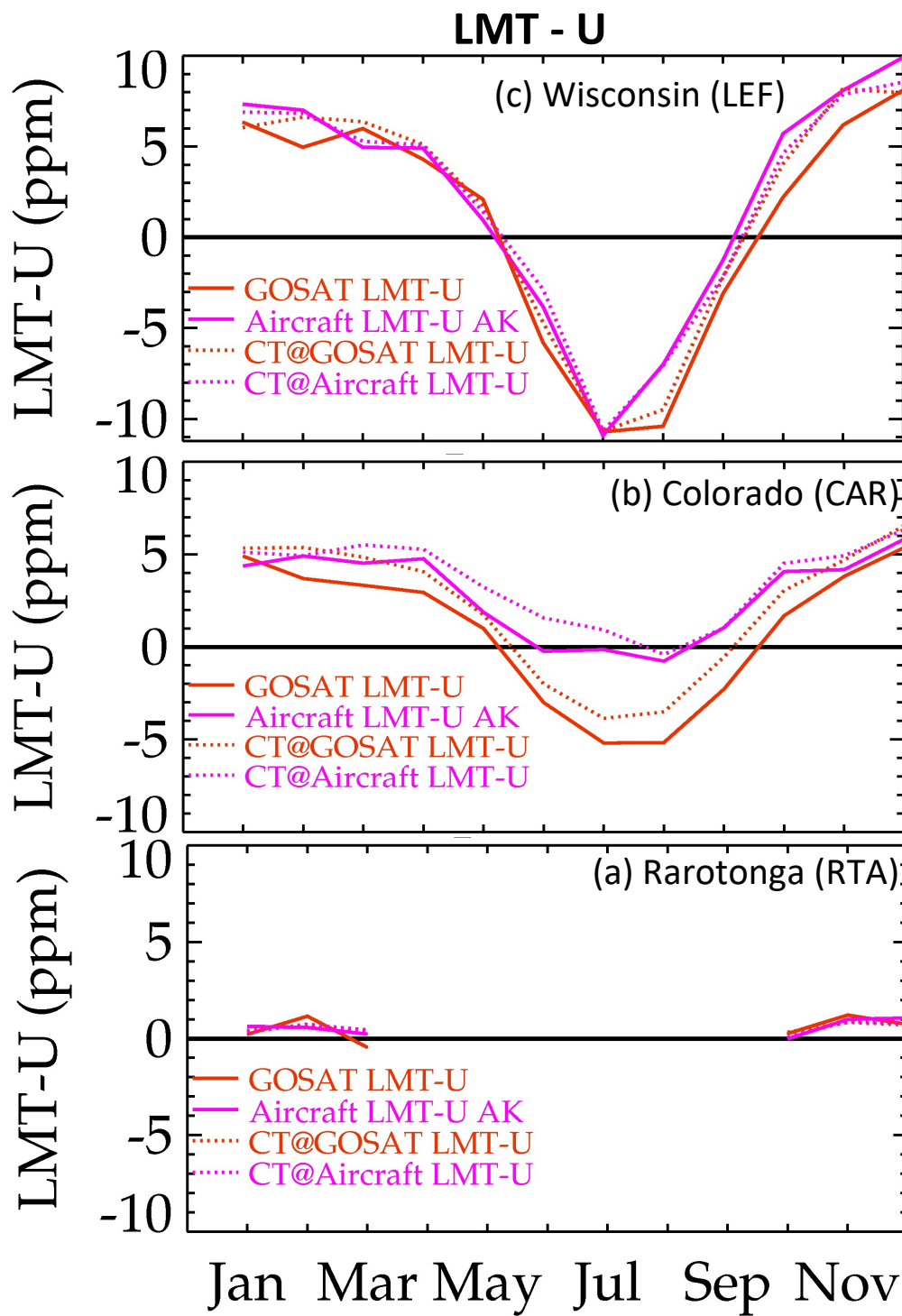


Figure 11. GOSAT LMT - U (red) versus aircraft (pink) at 3 sites. The dotted line show CarbonTracker matched to GOSAT (red dotted) or aircraft (pink dotted). Co-location error explains the discrepancies in the drawdown at CAR and LEF. At CAR the discrepancies are due to mismatch in the time of day the data is collected.

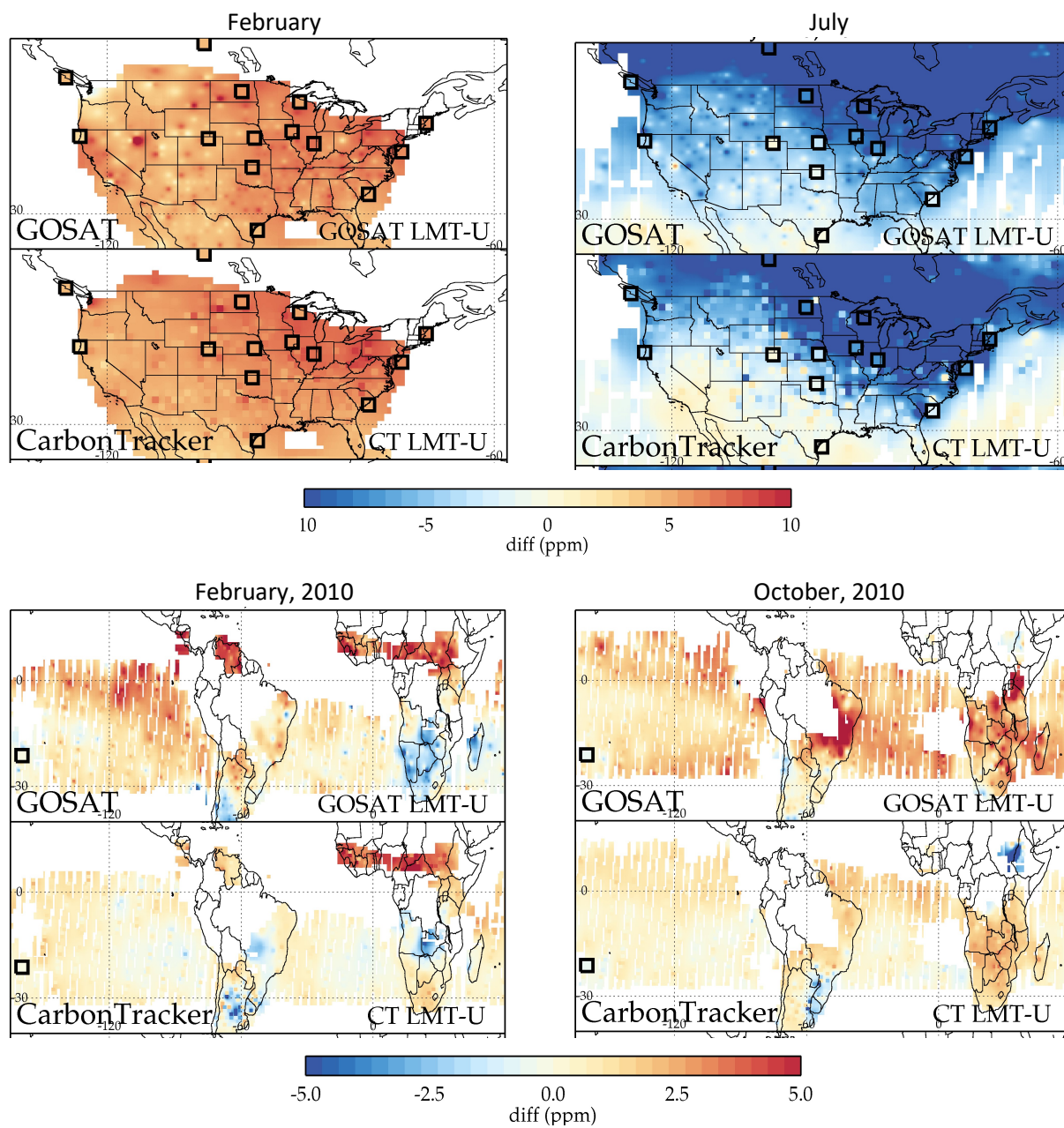


Figure 12. LMT – U differences. Results shown for the U.S. (top) and South America/Africa (bottom) for two different months, with GOSAT on the top and CarbonTracker on the bottom. Aircraft LMT – U differences are shown in the squares. There is agreement in the U.S. other than southwestern U.S. in July, with more differences in the southern hemisphere.